Radiatively Cooled Magnetic Reconnection Experiments Driven by Pulsed Power

R. Datta,[1] K. Chandler,[2] C. E. Myers,[2, a)] J. P. Chittenden,[3] A. J. Crilly,[3] C. Aragon,[2] D. J. Ampleford,[2] J. T. Banasek,[2] A. Edens,[2] W. R. Fox,[4] S. B. Hansen,[2] E. C. Harding,[2] C. A. Jennings,[2] H. Ji,[4] C. C. Kuranz,[5] S. V. Lebedev,[3] Q. Looker,[2] S. G. Patel,[2] A. Porwitzky,[2] G. A. Shipley,[2] D. A. Uzdensky,[6] D. A. Yager-Elorriaga,[2] and J.D. Hare *[1]

1)*Plasma Science and Fusion Center, Massachusetts Institute of Technology, MA 02139, Cambridge, USA*
2)*Sandia National Laboratories, Albuquerque, NM 87123-1106, USA*
3)*Blackett Laboratory, Imperial College London, London SW7 2BW, UK*
4)*Princeton Plasma Physics Laboratory, Princeton, NJ 08543, USA*
5)*Department of Nuclear Engineering and Radiological Sciences, University of Michigan, Ann Arbor, MI 48109, USA*
6)*Center for Integrated Plasma Studies, Physics Department, UCB-390, University of Colorado, Boulder, Colorado, USA*

(*Electronic mail: jdhare@mit.edu)

We present evidence for strong radiative cooling in a pulsed-power-driven magnetic reconnection experiment. Two aluminum exploding wire arrays, driven by a 20 MA peak current, 300 ns rise time pulse from the Z machine (Sandia National Laboratories), generate strongly-driven plasma flows ($M_A \approx 7$) with anti-parallel magnetic fields, which form a reconnection layer ($S_L \approx 120$) at the mid-plane. The net cooling rate far exceeds the Alfvénic transit rate ($\tau_{\text{cool}}^{-1}/\tau_{\text{A}}^{-1} \gg 1$), leading to strong cooling of the reconnection layer. We determine the advected magnetic field and flow velocity using inductive probes positioned in the inflow to the layer, and inflow ion density and temperature from analysis of visible emission spectroscopy. A sharp decrease in X-ray emission from the reconnection layer, measured using filtered diodes and time-gated X-ray imaging, provides evidence for strong cooling of the reconnection layer after its initial formation. X-ray images also show localized hotspots, regions of strong X-ray emission, with velocities comparable to the expected outflow velocity from the reconnection layer. These hotspots are consistent with plasmoids observed in 3D radiative resistive magnetohydrodynamic simulations of the experiment. X-ray spectroscopy further indicates that the hotspots have a temperature (170 eV) much higher than the bulk layer ($\leq$ 75 eV) and inflow temperatures (about 2 eV), and that these hotspots generate the majority of the high-energy ($>$ 1 keV) emission.

I. Introduction

Magnetic reconnection, a ubiquitous process in magnetized plasmas, is responsible for many highly energetic events in our Universe, such as solar flares and coronal mass ejections in our solar system,[1–3] reconnection events in the coronae of other stars, in the accretion disks and jets of Young Stellar Objects (YSOs),[4–6] and in the interstellar medium.[7–10] Reconnection occurs when anti-parallel magnetic field lines advected by plasma flows generate a current sheet, also known as a reconnection layer. In the current sheet, the frozen-in flux condition breaks locally, allowing an abrupt reconfiguration of the magnetic field topology.[3,11,12] This process explosively converts magnetic energy into thermal and kinetic energy inside the reconnection layer.

Because of the dissipation of magnetic energy as heat, radiative emission is often the key, and sometimes the only, observable signature of reconnection in many astrophysical systems, such as in solar and YSO flares.[5,13–15] Reconnection is also a proposed mechanism to explain the bursts of transient high-energy radiation observed from extreme relativistic astrophysical objects, such as black hole accretion disks and their coronae,[16–19] γ-ray bursts,[20–24] and pulsar magnetospheres and winds.[25–29] In astrophysical systems with strong reconnection-driven radiative emission, radiative cooling can be significant enough to rapidly remove internal energy from the system.[14,15,23] In particular, radiative cooling becomes important when the cooling rate τ_{cool}^{-1} dominates the Alfvén transit rate τ_A^{-1} in the reconnection layer, resulting in a large cooling parameter $R_{\text{cool}} \equiv \tau_{\text{cool}}^{-1}/\tau_A^{-1} \gg 1$. Here, $\tau_{\text{cool}} \equiv p/[(\gamma-1)P_{\text{cool}}]$ is the internal energy density $p/(\gamma-1)$ divided by the net volumetric cooling rate P_{cool}, and $\tau_A \equiv L/V_{A,in}$, where L is the layer half-length, γ is the adiabatic index, and $V_{A,in}$ is the Alfvén speed, calculated just outside the layer. In this regime, the plasma cools significantly before being ejected from the reconnection layer.

The ubiquity of radiative emission in astrophysical plasmas has motivated theoretical and numerical investigation into radiatively-cooled magnetic reconnection.[15,17,18,23,30–41] Building on earlier work by Kulsrud and Dorman,[30] Uzdensky and McKinney[23] presented the first theoretical description of radiatively-cooled Sweet-Parker-like reconnection. In this theory, the loss of internal energy via radiative emission cools the reconnection layer, leading to compression by the upstream magnetic pressure. This in turn increases the radiative emission rate. When an increase in layer compression causes radiative losses to increase faster than Ohmic dissipation, rapid runaway compression and cooling of the reconnection layer occurs; this process is termed radiative collapse.[23,30] Uzdensky and McKinney[23] showed that the Sweet-Parker reconnection rate is modified by a factor equal to the square root of the density compression ratio A, i.e. $E/V_{A,in}B_{in} \sim A^{1/2}S_L^{-1/2}$. Here, E and B_{in} are the reconnecting electric and magnetic fields respectively. The lower layer temperature results in a smaller (Spitzer) resistivity $\eta \sim T^{-3/2}$. Because of the strong

---

[a] Current address: Commonwealth Fusion Systems, Devens, MA 01434, USA

compression ($A \gg 1$) and lower temperature (hence, lower Lundquist number $S_L = V_{A,in}L/\bar{\eta}$), this theory predicts an increased reconnection rate due to radiative collapse.[23]

Numerical simulations of astrophysical systems in the non-relativistic resistive MHD regime show evidence for this cooling-driven compression of the reconnection layer,[30,42–45] consistent with theoretical predictions. More recently, this effect has also been observed in radiative-PIC (particle-in-cell) simulations of relativistic magnetic reconnection, which model reconnection physics in strongly-cooled extreme astrophysical systems exhibiting synchrotron and/or inverse external Compton cooling.[18,31–41] Simulations of current sheets unstable to the plasmoid instability in electron-positron pair plasmas cooled via synchrotron emission have additionally shown cooling-driven compression of the density and reconnected magnetic flux inside magnetic islands or 'plasmoids',[46,47] making them sites of enhanced radiative emission in the current sheet.[35,36]

Despite various numerical studies, experimental investigation of radiatively-cooled reconnection remains largely unexplored, in part due to the difficulty in achieving the cooling rates necessary for observing radiative collapse on experimental time scales. Yamada, Kulsrud, and Ji provide a review of major laboratory experiments of magnetic reconnection.[3] The earliest experimental validation of Sweet-Parker theory in a laboratory experiment was provided by the Magnetic Reconnection eXperiment (MRX), which generated a quasi-2D collision-dominated $S_L > 10^3$ reconnection layer in a toroidally symmetric geometry.[48,49] MRX, and other magnetically-driven devices such as TREX,[50,51] access a low-density magnetically-dominated regime ($n_e \sim 10^{12} - 10^{13}\,\text{cm}^{-3}$, $T_e \sim 10\,\text{eV}$, $\beta \ll 1$) where radiative cooling is negligible. These experiments have provided significant insight into a variety of reconnection physics, such as evidence for strong ion heating,[52] two-fluid effects and Hall reconnection,[50,51,53] as well as magnetic flux pile-up.[51]

In contrast to low-β magnetically-driven experiments, laser-driven experiments of magnetic reconnection provide access to a strongly-driven $\beta \gg 1$ high-energy-density (HED) regime ($n_e \sim 10^{20}\,\text{cm}^{-3}$, $T_e \sim 1000\,\text{eV}$).[54,55] In these experiments, adjacent sub-millimeter spots on a solid target are irradiated with an intense Terawatt-class laser beam. The reconnecting magnetic fields are either self-generated by the Biermann battery effect,[54,56–58] or supplied via external coils[59] or laser-driven capacitor coils.[60] Laser-driven experiments have provided evidence for two-fluid effects,[54,58,59] magnetic flux pile-up,[59] and particle acceleration in magnetic reconnection.[60] However, despite the high operating pressure, the cooling parameter in these experiments was small as the plasma ions become fully-stripped at these high temperatures,[55–57] eliminating strong cooling by atomic transitions.

Pulsed-power-driven experiments are another class of strongly-driven $\beta \approx 0.1 - 1$ HED magnetic reconnection experiments.[61] In these experiments, a strong (~ 1 MA peak currrent peak currrent) time-varying ($100 - 250\,\text{ns}$) current pulse simultaneously drives two cylindrical exploding wire arrays placed side-by-side.[62–66] Each wire array generates

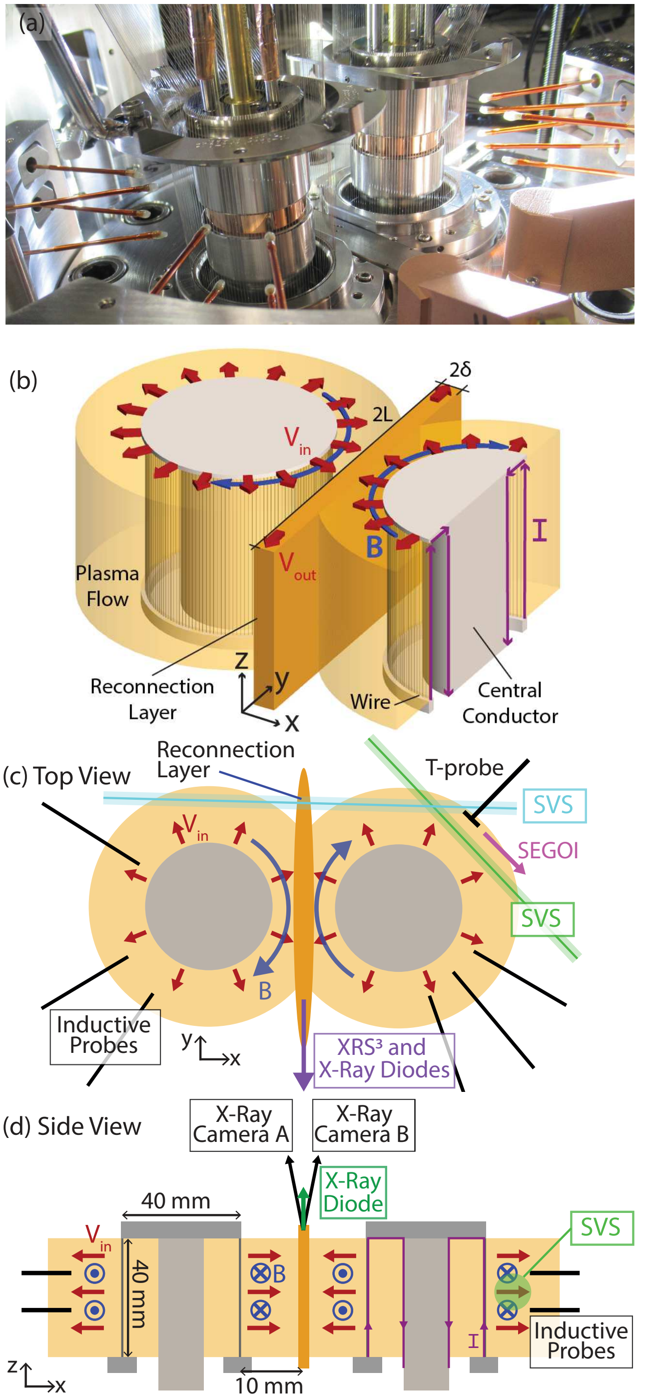

FIG. 1: (a) In-chamber image of the MARZ load hardware. (b) A 3D schematic of the MARZ load hardware, showing two exploding wire arrays, each with 150, 75 µm diameter aluminum wires. Each array generates radially-diverging plasma flows (red) with frozen-in magnetic fields (blue), that generate a reconnection layer at the $x = 0$ midplane. (c) Top (xy-plane) view of the load, showing the arrangement of inductive probes (black), and lines-of-sight of streaked visible spectroscopy (SVS) [green, blue], X-ray spectroscopy (XRS^3) and side-on X-ray diodes (purple), and the self-emission gated optical imager (SEGOI) [magneta]. (d) Side (xz-plane) view of the load, showing the lines-of-sight of the end-on X-ray diode (green), and the two X-ray cameras (black).

radially-diverging (with respect to the array center) flows of magnetized plasma, which collide in the mid-plane, generating a reconnection layer. Experiments on the MAGPIE facility ($n_e \sim 10^{18}\,\mathrm{cm}^{-3}$, $T_e \sim 50\,\mathrm{eV}$) using aluminum wires demonstrated cooling of the ions at a low $S_L < 10$, measured via collective spatially-resolved optical Thomson scattering.[62,67] Using lower-Z carbon wires, these experiments accessed higher Lundquist numbers $S_L \sim 100$,[63,64] at which plasmoid formation was observed, unlike in the lower Lundquist number aluminum experiments.[62,67] However, in these carbon experiments, there was negligible cooling of the reconnection layer, as the carbon ions were fully stripped.

In this paper, we present results from the Magnetic Reconnection on Z (MARZ) experiments, which build on previous pulsed-power experiments and simultaneously demonstrate both a high $S_L \approx 120$ and a high cooling parameter $R_{\mathrm{cool}} \sim 50$. The MARZ experimental platform generates a radiatively-cooled reconnection layer by driving a dual exploding wire array using the Z machine (20 MA peak current, 300 ns rise time, Sandia National Labs).[68] The reconnection layer undergoes strong cooling, which is characterized by the rapid decline in X-ray emission generated from the layer. Furthermore, high-energy emission from the layer is dominated by localized fast-moving hotspots, which are consistent with magnetic islands produced by the plasmoid instability[36,46,47] which were seen in three-dimensional resistive magnetohydrodynamic simulations of the experiment.[69] These experiments provide the first quantitative measurements of reconnection and plasmoid formation in a strongly radiatively-cooled regime, and directly characterize the high-energy radiative emission from the reconnection layer, using temporally- and spatially-resolved X-ray diagnostics. This, as mentioned earlier, is of particular astrophysical significance, because of the generation of high-energy emission in reconnecting astrophysical systems.[14,15]

Two- and three-dimensional radiative resistive magnetohydrodynamic (MHD) simulations of the MARZ experiments were previously reported in Ref. 69. The simulations were performed using GORGON — an Eulerian resistive MHD code with van Leer advection.[70,71] The simulations implemented both volumetric radiative loss and $P_{1/3}$ multi-group radiation transport, using spectral emissivity and opacity tables generated by the atomic code SpK.[72] Line emission dominated in the simulations, providing strong cooling of the reconnection layer. Key results from these simulations are summarized as follows — (1) strong radiative cooling ($R_{\mathrm{cool}} \approx 100$) drove radiative collapse of the current sheet, resulting in decreased layer temperature and strong compression; and (2) the current sheet was unstable to the plasmoid instability, forming strongly-emitting plasmoids in the reconnection layer, which eventually collapsed due to radiative cooling.[69] In this paper, we additionally compare our experimental findings with results from these simulations. Our previous paper[73] provided details on the X-ray diagnostic results from these experiments; this present paper not only expands on the X-ray results, but also contributes results from additional diagnostics, providing context and further characterization of these experiments.

This paper is structured as follows. In §II, we describe the load hardware and the experimental diagnostics. Results from the experiments are described in §III, while analysis of experimental data and discussion of key results, including radiative cooling and plasmoid formation, are provided in §IV. Finally, we outline key conclusions and future work in §V.

II. Experimental and Diagnostic Setup

A. MARZ Load Hardware

Figure 1(a-b) show the load hardware. The load consists of two cylindrical exploding arrays, each with 150 equally-spaced, 75 µm diameter aluminum wires. The array diameter is 40 mm, and the array height is 36 mm. The center-to-center separation between the arrays is 60 mm, giving a 10 mm distance between the wires and the mid-plane. Both wire arrays are over-massed, so they generate continuous plasma flows throughout the experiment without exploding.[74,75] A scaled experiment that matched the current per wire and driving magnetic field of the MARZ experiment was reported in Ref. 75, using a single planar wire array on the 1 MA COBRA machine. Results from these experiments show good ablation from 75 µm diameter Al wires, with no closure of the inter-wire and the cathode-wire gaps.[75]

The Z machine[68] drives a 20 MA peak, 300 ns rise time current pulse through the load, which has an inductance of about 2.5 nH. When current flows through the wires, the wires heat up resistively, and the wire material vaporizes and ionizes to create low-density coronal plasma surrounding the dense wire cores. Current density is concentrated within a thin skin region which generates coronal plasma around the stationary cores. The driving magnetic field points azimuthally inside the cathode-wire gap of each array, and rapidly drops to zero outside the array.[76] The global $\mathbf{j} \times \mathbf{B}$ force, therefore, accelerates the coronal plasma radially outwards from each array, and the ablated plasma streams supersonically and super-Alfvénically into the vacuum region outside the arrays. The ablating plasma advects magnetic field from inside the cathode-wire gap to the outside, resulting in radially-diverging flows of magnetized plasma.[77] The plasma flows from each array advect frozen-in magnetic field to the mid-plane, where the field lines are anti-parallel and generate a reconnection layer (see Figure 1).

Three MARZ shots (MARZ1, MARZ2, and MARZ3) have been conducted on the Z machine so far. Each shot was fielded with identical load hardware and driving conditions, and an evolving set of diagnostics, as detailed in §II B.

B. Diagnostic Setup

Figure 1(c-d) show the diagnostic setup. We categorize the diagnostics into current, inflow, and reconnection layer diagnostics. Current diagnostics, which include B-dot probes in the magnetically insulated transmission line (MITL) of the Z machine and Laser Photonic Doppler Velocimetry (PDV), monitor current delivery to the load. Inflow diagnostics, which include inductive probes and streaked visible spectroscopy, characterize the plasma ablating from the wires, which in turn, form the inflows into the reconnection layer. Finally, the reconnection layer diagnostics characterize the plasma in the current sheet, and consist of filtered X-

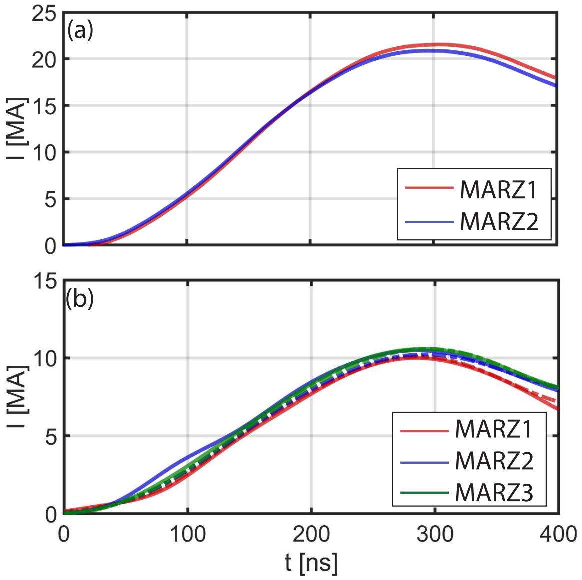

FIG. 2: (a) Averaged current measured by B-dot probes in the magnetically insulated transmission line (MITL) of the Z machine for two different shots (MARZ1 - red; MARZ2 - blue). The peak current is about 21 MA, and the rise time is about 300 ns. (b) Current measured by Photonic Doppler Velocimetry (PDV) in the east (solid) and west (dashed) arrays, showing equal current division between both arrays on all three shots.

ray diodes, X-ray imaging, and time-integrated X-ray spectroscopy. We provide more details on each diagnostic below.

1. *Current Diagnostics*

Dual-polarity B-dot probes in the MITL of the Z machine monitor the load current.[78] These probes are calibrated, and their signals are numerically integrated to determine the current. PDV[78,79] is used to monitor the current delivered to each individual wire array. PDV tracks the velocity of a copper flyer plate which forms a section of the central conductor of each array, which accelerates due to the driving magnetic pressure.[78] A comparison of the measured flyer plate velocity with 1D-MHD simulations is used to calculate the delivered current. Each array contains 4 separate PDV probes which record the flyer plate velocity at different azimuthal locations around the central conductor. The MITL B-dots and PDV are routinely fielded on the Z machine to characterize power flow; details of these systems are provided in Ref. 78.

2. *Inductive probes*

We position inductive probes at multiple radial locations around the wire arrays to measure the time- and space-resolved magnetic field advected by the plasma ablating from the wires. Each inductive probe consists of a single-turn loop created by connecting the inner conductor of a coaxial cable (2 mm outer diameter) to the outer conductor.[80] In MARZ1, inductive probes were positioned at radial distances of 5 mm, 8 mm, 11 mm, and 14 mm from the wires, with the normals to the wire loops parallel to the azimuthal magnetic field. In MARZ2 and MARZ3, the probes were at 5 mm, 10 mm, and 20 mm. The probes at different radii are at different azimuthal locations (see Figure 1c); however, the azimuthal variation in the measured magnetic field is expected to be small due to cylindrical symmetry.[77,81–83] We position two probes of opposite polarity at each location, separated vertically by 1 cm (see Figure 1d). This allows us to eliminate the contribution of electrostatic voltages via common mode rejection.[81,83] Each probe is calibrated before use, and we numerically integrate the signals to determine the magnetic field.

3. *Streaked Visible Spectroscopy*

Streaked visible spectroscopy (SVS)[78,84] makes measurements of visible emission spectra from the plasma, along paths in the xy plane, as shown in Figure 1c. Optical fibers collect and transmit light to a spectrometer (1 m McPherson Model 2061 scanning monochromator; 140 mm × 120 mm, 50 G/mm, 6563 Å blaze diffraction grating) and a streak camera (Sydor streak camera; SI-800 CCD) setup. The tip of each fiber (Oz Optics, LPC-06-532-105/125-QM-0.8-1.81CL) consists of a MgF_2 anti-reflection coated collimating lens ($f = 1.85\,\mathrm{mm}$, $\mathrm{NA} = 0.22$). The beam divergence is 57 mrad, resulting in a spot diameter of about 5 mm at the center of the collection volume. The spectral range and resolution of the system are 300 nm and 1.5 nm respectively. The sweep time is about 550 ns, and the temporal resolution is 0.3 ns. In MARZ1, we simultaneously record emission from the plasma ablating from the backside of the arrays at 8 mm and 17 mm from the wires (green line in Figure 1c), using separate SVS systems. In MARZ3, the visible spectroscopy line-of-sight (LOS) includes plasma ablating from both arrays and the plasma in the reconnection layer (blue line in Figure 1c), along $y = 26.5\,\mathrm{mm}$ and $y = 34\,\mathrm{mm}$.

4. *Visible Self-Emission Imaging*

In MARZ1, we positioned an additional inductive probe with a 10 mm long 1 mm diameter glass rod attached to its tip, at 15 mm from the wires (hereafter, referred to as the 'T-probe') (see Figure 1c). It provides an extended obstacle that creates a detached bow shock when the flow interacts with the probe. We observe the bow shock using a self-emission gated optical imager (SEGOI).[78] SEGOI is an 8-frame camera that records 2D self-emission images in the visible range (540-650 nm) on 8 separate micro-channel plates (MCPs). We record images between 320-367 ns, with a 7 ns inter-frame time, 1 ns exposure, and a 8 mm diameter field of view. SEGOI also captures a 1D streak image (sweep time = 300-400 ns) along a line parallel to the T-probe axis, 2 mm below the probe.

5. *X-Ray Diodes*

Silicon diodes[78] record the X-ray power generated from the reconnection layer. In MARZ1 and MARZ2, the diode viewed the reconnection layer from the side (side-on). The diode was filtered with 2 µm of aluminized Mylar (Figure 1c). The $T = 0.5$ transmission cut-off for this filter is at about 100 eV. In MARZ3, the diode viewed the reconnection layer from the top (end-on) [Figure 1d], and was filtered with 8 µm-thick beryllium. The $T = 0.5$ cut-off is at roughly 1 keV. Each diode has a 22.5 µm active layer and a nominal 0.6 mm diameter. The diode response is 0.276 A/W.

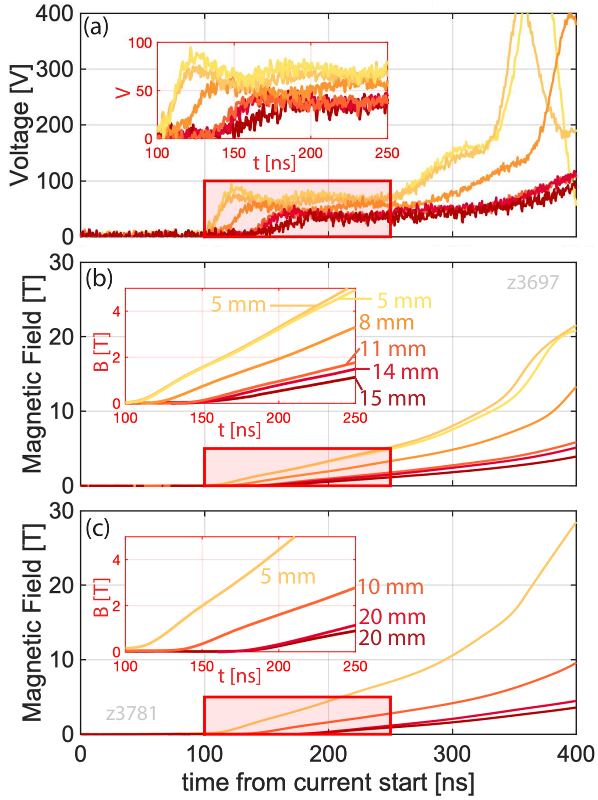

FIG. 3: (a) Inductive voltage signals from probes placed at radial distances 5, 8, 11, 14, and 15 mm from the wires in MARZ1. Signals are delayed with respect to one another due to the transit time of the magnetic field advected by the plasma between the probe locations. (b) Time-resolved magnetic field measurements at different radii around the array in MARZ1. (c) Magnetic field measurements in MARZ3.

6. X-Ray Imaging

We image the reconnection layer using two time-gated ultra-fast X-ray imaging (UXI) cameras.[78] The cameras provide a $25 \times 12.5\,\text{mm}^2$ (1025px × 512px) field of view through a $500\,\mu\text{m}$ diameter pinhole (magnification = 1×, geometric resolution $\approx 1\,\text{mm}$). The cameras view the reconnection layer with polar angles of $\theta = 9^\circ$ and $\theta = 12^\circ$ with respect to the z-axis (see Figure 1d), and with azimuthal angles (from the $x-$axis) of $\phi = 170^\circ$ and $\phi = 40^\circ$ (not shown in Figure 1), thus viewing both the top and side of the layer. The pinholes are filtered with $2\,\mu\text{m}$ thick aluminized Mylar, which filters out photons with energies $< 100\,\text{eV}$. Each camera records 4 images with a 20 ns inter-frame time, and a 10 ns exposure time. Data from this diagnostic is only available for MARZ3.

In addition to time-gated imaging, we record time-integrated X-ray images of the reconnection layer, using two pinhole cameras viewing the layer from the top with polar angles of roughly 5°. Pinhole diameters of $300\,\mu\text{m}$ and $500\,\mu\text{m}$ are used. Each camera has 3 pinholes of the same diameter but different filtration that generate three images (magnification ≈ 0.5, resolution $\approx 450 - 750\,\mu\text{m}$) of the reconnection layer on a 64 mm × 34 mm image plate.

7. Time-integrated X-Ray Spectroscopy

An X-ray scattering spectrometer (XRS^3)[78,85] with a spherically-bent quartz crystal provides time-integrated spatially-resolved (along the out-of-plane z direction, resolution: $\Delta z \approx 200\,\mu\text{m}$) measurements of X-ray emission spectra from the reconnection layer. The range and spectral resolution of the spectrometer in the MARZ experiments were 1.5-1.9 keV and $\Delta E \approx 0.5\,\text{eV}$ respectively. We record the X-ray spectrum on an image plate (Fuji TR), filtered with a $11\,\mu\text{m}$ thick beryllium filter. Data was recorded in either of two configurations — (1) 150 mm radius crystal, crystal-to-target separation = 800 mm, and a $8\,\mu\text{m}$ kapton filter on the spectrometer entrance slit; and (2) 200 mm radius crystal, crystal-to-target separation = 500 mm, and no kapton filter. Configuration 1 was used for MARZ1 and MARZ2, while configuration 2 was used for MARZ3.

III. Results

We describe the experimental results from our diagnostics in this section. In MARZ2, damage to one of the arrays during installation produced results which were unreproducible. Therefore, we show results primarily from MARZ1 and MARZ3, with some exceptions.

A. Current Measurements

Figure 2a shows the averaged current measured by the MITL B-dot probes in MARZ1 and MARZ2. The Z machine consistently delivered a peak current of roughly 21 MA, with a rise time of about 300 ns across the two shots. The shot-to-shot variation in the delivered current was $< 5\%$.

Figure 2b shows the current measured by the PDV diagnostic for all three shots. We show the averaged current for the east (solid line) and west (dashed line) arrays in each shot. Figure 2b shows equal current division between the arrays. As expected, the shape of the current pulse measured by PDV matches that of the current measured by the MITL B-dots. The peak value in each array is roughly 10 MA, showing negligible current loss between the MITL and the load. Current measurements by the MITL B-dot probes are not available for MARZ3, but the PDV measurements in Figure 2b show that the current delivered to the load in this shot was consistent with the other two shots.

B. Magnetic Field and Velocity in the Inflow Region

Figure 3a shows the voltage signals from probes in MARZ1. We only show the inductive component of the signals $\bar{V} = 0.5(V_+ - V_-)$, determined from common mode rejection of signals from the two opposite-polarity probes at each location. The signals in Figure 3a are all similar in shape, but displaced in time, which is expected due to the advection of the frozen-in magnetic field by the plasma between the locations of the probes.[77,83] We note that the probes are placed on the side of the arrays opposite to that of the reconnection layer (as shown in Figure 1), so they measure the 'unperturbed' magnetic field in the inflow, not affected by reconnection.

We numerically integrate the signals in Figure 3a to determine the magnetic field, as shown in Figure 3b. The advected magnetic field increases with time, due to a rise in the driving current, and decreases with distance from the wires, consistent

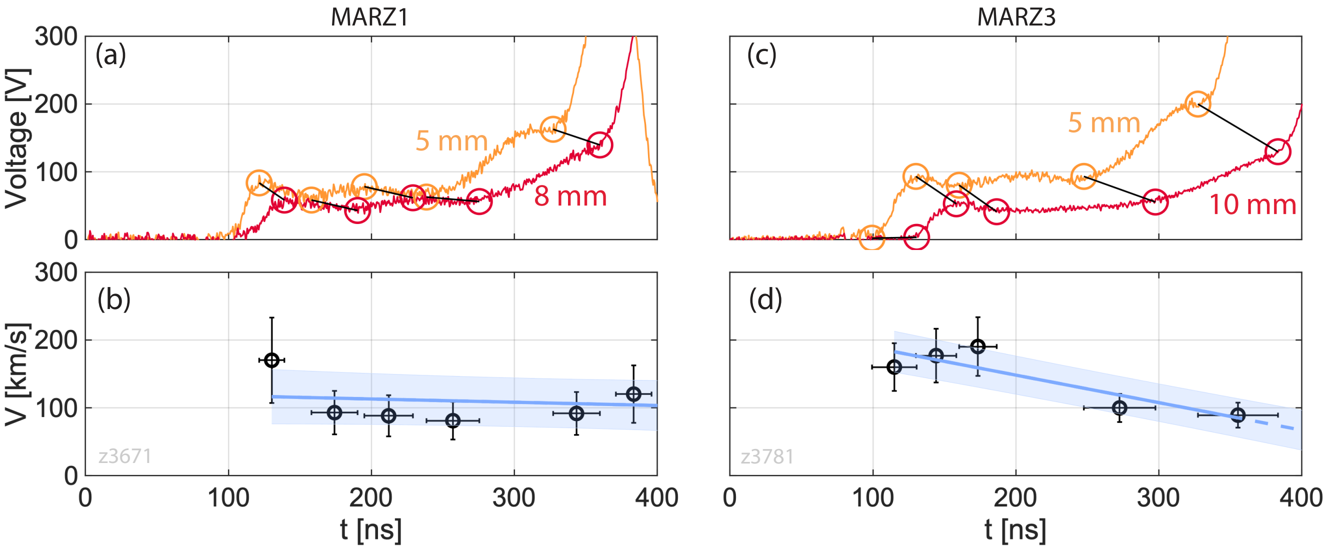

FIG. 4: (a) Inductive voltage signals from probes placed at 5 mm and 8 mm from the wires in MARZ1, showing delay between the signals. (b) Estimate of the average flow velocity between 5-8 mm from the time delay of the inductive probe signals in MARZ1. (c) Inductive voltage signals from probes placed at 5 mm and 10 mm from the wires in MARZ3. (d) Estimate of the average flow velocity between 5-10 mm from the time delay of the inductive probe signals in MARZ3. The error bar in velocity is derived from propagating the uncertainties in the probe separation and the transit time, while the error bar in time represents the time interval over which the velocity is calculated.

with previous measurements in exploding wire arrays.[77,81–83] In Figure 3b, two separate probes at 5 mm from the wires record the magnetic field from different arrays. Both probes exhibit similar magnetic fields, consistent with equal current splitting between the arrays, as described in §III A.

Figure 3c shows the magnetic field recorded in MARZ3. The recorded magnetic field is slightly larger than that in MARZ1. Here, inductive probes measuring the magnetic field from the two arrays at 20 mm from the wires show identical magnetic fields, consistent with equal current splitting. We note that in MARZ3, the two opposite-polarity probes at 5 mm recorded significantly different signals. The signal on the bottom probe was consistent with the expected field magnitude (based on measurements in MARZ1), while the other was anomalously high. Therefore, we discard the anomalous signal and only report data from one probe at 5 mm in Figure 3c.

Finally, we note that probes measuring the advected magnetic field from different arrays at the same radial distance in MARZ2 measured significantly higher advected magnetic field on the west array, despite equal current splitting observed in Figure 2b. The west array was partly damaged during installation on this shot, and the probes were measuring the magnetic field from the damaged section of the array.

The delay in the voltage signals between probes at different locations provides an estimate of the average flow velocity.[83] Figure 4a shows the voltage signals recorded by probes in MARZ1 at 5 mm and 8 mm respectively. The signals show several identifiable features, indicated via circles in Figure 4a. By tracking the transit time of these features, we estimate the flow velocity, as shown in Figure 4b. The flow velocity is roughly 110 km s^{-1}, consistent with flow velocities previously recorded in pulsed-power-driven wire arrays.[61,66] In Figure 4c, we show the inductive probe voltage measurements at 5 mm and 10 mm from the wires for MARZ3, together with the estimated flow velocity in Figure 4d. On this shot, the recorded flow velocity varied between $100-200$ km s^{-1}.

C. Measurements of Visible Spectra in the Inflow

Figure 5 shows streak images of the visible emission spectra collected at 8 mm and 17 mm from the wires respectively in MARZ1. Note that these spectra are from the side of the wire arrays opposite the reconnection layer (see Figure 1c). We have applied corrections to these spectra for distortions by streak camera optics, timing corrections for spectral differences in photon transit delay over the fiber length, as well as relative intensity corrections due to the wavelength-dependent response of the spectrometer.[84] Wavelength calibration and instrument broadening (about 1.5 nm) were determined using preshot images of 458 nm and 543 nm laser lines recorded by each SVS system.

The streak camera first records emission at roughly 90 ns for the 8 mm system (Figure 5a). This corresponds to an average flow velocity of roughly 90 km s^{-1} between the wire and probe locations; the estimated velocity is consistent with that estimated from inductive probe measurements (Figure 4). Compared to the spectra at 8 mm, emission at 17 mm is first recorded later at roughly 140 ns, corresponding to an average velocity of roughly 120 km s^{-1} (Figure 5c). Finally, by integrating the spectral intensity in wavelength space, we find that the temporal evolution of intensity $\int I(\lambda) d\lambda$ (which depends on the plasma density) roughly matches that of the advected magnetic field shown in Figure 3.

Figure 5(b and d) show lineouts of the streak images at different times, each averaged over 10 ns. The spectra at both radial locations show well-defined Al-II and Al-III emission lines, which correspond to transitions in singly- and doubly-ionized aluminum respectively. Later in time, continuum

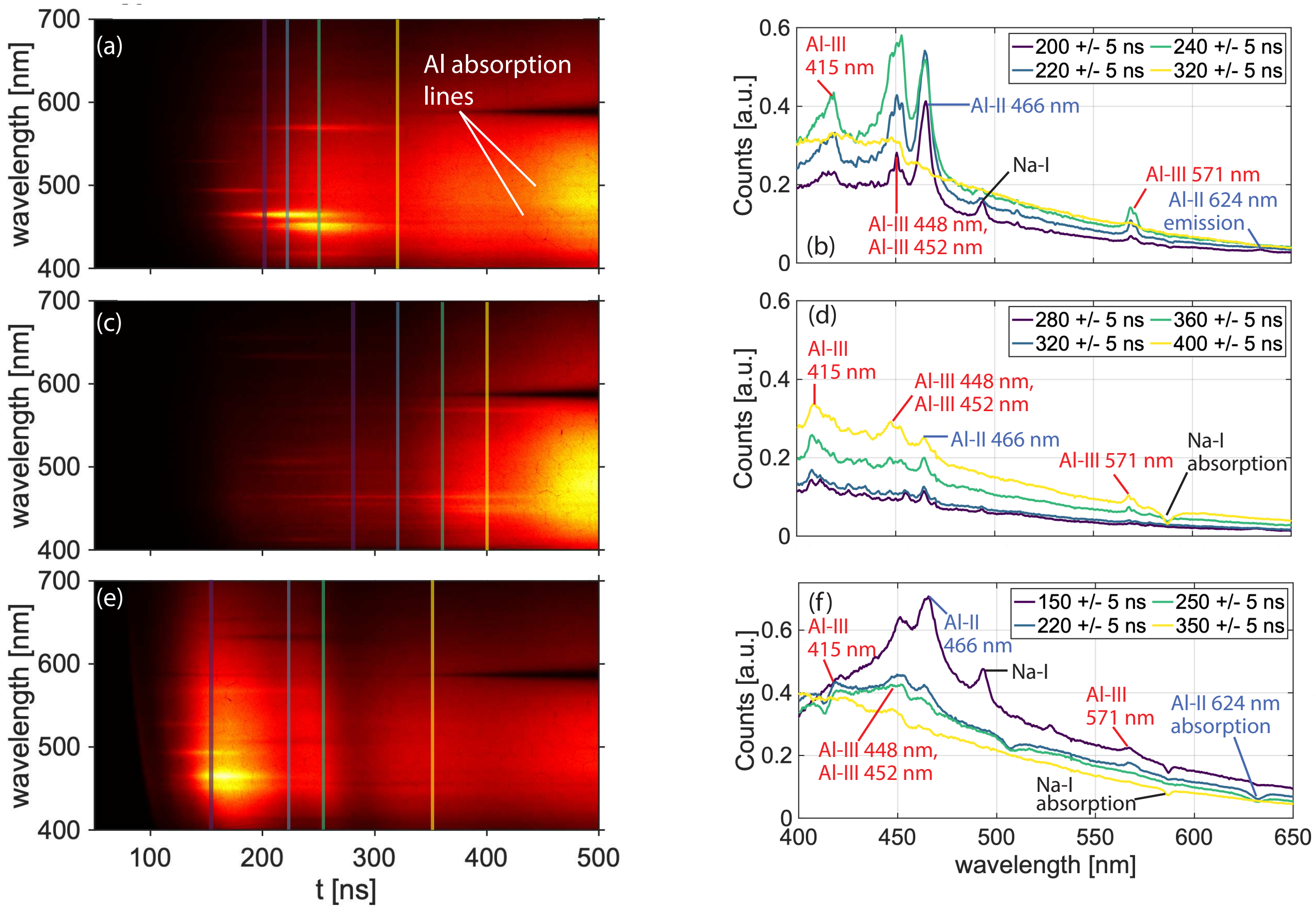

FIG. 5: Streaked visible spectrum recorded (a) 8 mm from the wires and (c) 17 mm from the wires in MARZ1. (b) The visible spectrum at $t = 200, 220, 240$ & 320 ns at 8 mm from the wires. (d) The visible spectrum at $t = 280, 320, 360$ & 400 ns at 17 mm from the wires. These spectra are averaged over 10 ns. Identified emission lines are shown in (b) and (d). (e) Streaked visible spectrum in MARZ3. The diagnostic line of sight includes plasma in the reconnection layer and that ablating from the wires. (f) The visible spectrum at $t = 150, 220, 250$ & 350 ns averaged over 10 ns. The Al-II 624 nm line appears as an absorption feature.

emission begins to dominate over line emission. This occurs at around 300 ns and 450 ns for the 8 mm and 17 mm observations respectively. Late in time, the spectra also exhibit absorption features corresponding to Al-II and Al-III transitions, as indicated in Figure 5. We use the Al emission lines to estimate time-resolved values of ion density and electron temperature in the inflow region. This analysis, performed using collisonal-radiative and radiation transport modeling, is described in §IV B.

In MARZ3, the diagnostic LOS included plasma in the reconnection layer and that ablating from both wire arrays, as shown in Figure 1c (blue line). The spectra, shown in Figure 5(e-f), are similar to that recorded in MARZ1 (Figure 5), with well-defined Al-II and Al-III emission features. However, between 150-350 ns, the Al-II 624 nm transition, which appears as an emission line in Figure 5(a-d), now appears as an absorption feature in Figure 5(e-f). We discuss the origin of this absorption feature in §IV B.

In addition, the spectra exhibit features associated with the coatings on the optical components. The streak images show a stray Na-I line at roughly 485 nm early in time, as well as a strong Na-I absorption feature later in time. These features are not generated by the aluminum plasma, but are instead stray features generated from the optical coatings in the system. These stray features appear at around the same time in all streak images.

D. Bow shock Imaging

Figure 6 shows an optical self-emission image of the T-bar probe at 346 ns. A bow shock, which appears as a curved region of enhanced emission, forms around the T-probe. Shock formation around the T-probe provides visual confirmation of wire array ablation and generation of supersonic flow. Multi-frame self-emission images, as well as the 1D streak image of the bow shock, show that the shock front remains invariant in time between 300-400 ns. The shock angle, determined from the derivative of the shock front position (red curve in Figure 6), asymptotes to about 30°.

E. X-Ray emission from the reconnection layer

We now present results from the reconnection layer diagnostics, which characterize the temporal, spatial, and spectral properties of X-ray emission from the reconnection layer.

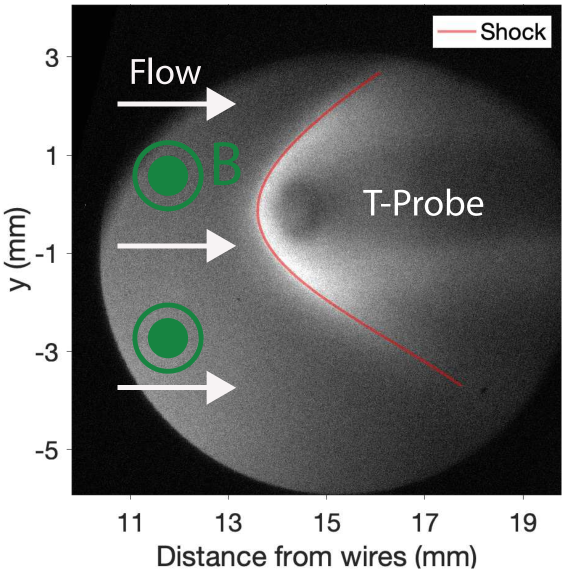

FIG. 6: Gated optical self-emission image of a bow shock around the T-probe. The bow shock exhibits a Mach angle of about 30°.

1. *X-Ray diodes*

The X-ray diodes characterize the temporal evolution of X-ray emission from the reconnection layer. Figure 7 shows the signals from the side-on (blue, grey) and end-on (red) diodes. All three diode signals exhibit a peak in X-ray emission at about 220 ns. For the side-on diodes, which measure $> 100\,\mathrm{eV}$ photons, the emission first ramps up around 150 ns, and the full-width-at-half-maximum (FWHM) of the signal is about $80-90\,\mathrm{ns}$. Similarly, the signal from the end-on diode, which records comparatively harder X-rays with energy $> 1\,\mathrm{keV}$, initially ramps up around 200 ns, and exhibits a FWHM of roughly 50 ns. The X-ray emission peaks around 220 ns on all diodes, and then falls sharply. The shape of the X-ray emission is much sharper than that of the driving current pulse, which peaks about 100 ns after the peak in X-ray emission (see Figure 2). This shows that the emission feature is related to the dynamics of the current sheet, rather than the driving current. In addition, the diodes consistently record a small emission feature at about 100 ns. This feature may be related to the initial arrival of plasma at the mid-plane.

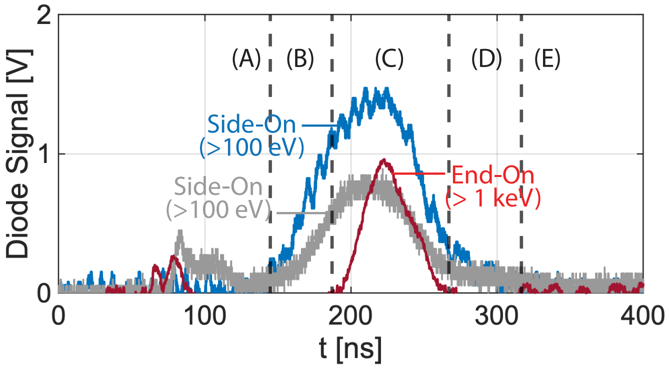

FIG. 7: X-ray power emitted from the reconnection layer as measured by the side-on (blue, gray) and end-on diodes (red).

2. *Time-gated X-ray Imaging*

Figure 8(a-b) shows time-gated images of the reconnection layer recorded in MARZ3. Camera A (polar angle $\theta = 9^\circ$, azimuthal angle $\phi = 170^\circ$) recorded images between 190-250 ns at 20 ns intervals, while camera B ($\theta = 12^\circ$, $\phi = 40^\circ$) recorded images between 180-240 ns, again at 20 ns intervals. Images from both cameras show an elongated layer of bright emission. The intensity of ($> 100\,\mathrm{eV}$) X-ray emission increases initially, consistent with the formation of the reconnection layer, and falls thereafter. Along with the brightness of the emission, the width of the emitting region (along x) also decreases with time. Peak emission is recorded between $210-220\,\mathrm{ns}$. By 250 ns, the emission has fallen significantly, and the layer is no longer visible on the X-ray cameras.

The X-ray images provide information about the spatial distribution of emission from the reconnection layer. Emission is highly inhomogeneous — Figure 8(a-b) shows sub-millimeter scale regions of enhanced emission embedded within the less brightly emitting layer. The intensity of emission from the hotspots is > 10 times higher than the average intensity from the rest of the layer. The presence of emission hotspots indicates localized regions of plasma with higher temperature or density relative to the rest of the layer.

These hotspots, indicated via green and yellow arrows in Figure 8(a-b), can be observed in images from both cameras to travel away from the center of the layer. We track the translation of the hotspot centroids between successive frames to estimate their velocities. Figure 9 shows the estimated hotspot velocity calculated using images from camera A between 220-240 ns (green), and from camera B between 190-210 ns (yellow). The hotspot velocities are consistent between both cameras. Hotspots accelerate along the $\pm y$-direction, away from the center of the layer. Hotspot velocity increases from $0\,\mathrm{km\,s^{-1}}$ to about $50\,\mathrm{km\,s^{-1}}$ over a distance of roughly 10 mm. We will show in §IV F that the observed hotspot velocity is consistent with the expected velocity of the outflows from the reconnection layer.

3. *Time-integrated X-ray Imaging*

Figure 8c shows a time-integrated X-ray image of the reconnection layer. The image is recorded with a 300 μm diameter pinhole, filtered with 2 μm aluminized Mylar, identical to the time-gated X-ray cameras in §III E 2. Figure 8c shows an elongated region of bright emission. The extent of the emission region in the $y-$direction is about 60 mm, while the FWHM along the $x-$direction is $1.6 \pm 0.5\,\mathrm{mm}$. The FWHM of the emitting region was determined by fitting a Gaussian function to the intensity variation along x at different $y-$positions. Here, we only show one of the recorded time-integrated X-ray images; however, the features of the image in Figure 8c are consistent with the other images recorded in the experiment.

4. *X-ray spectroscopy*

Figure 10(a-b) show the time-integrated spectrum of the X-ray emission from the reconnection layer for MARZ1 and MARZ3. Emission lines with energies 1570-1600 eV were observed in both shots. Although the output is time-integrated, the end-on diode signal (filtered with 8 μm Be),

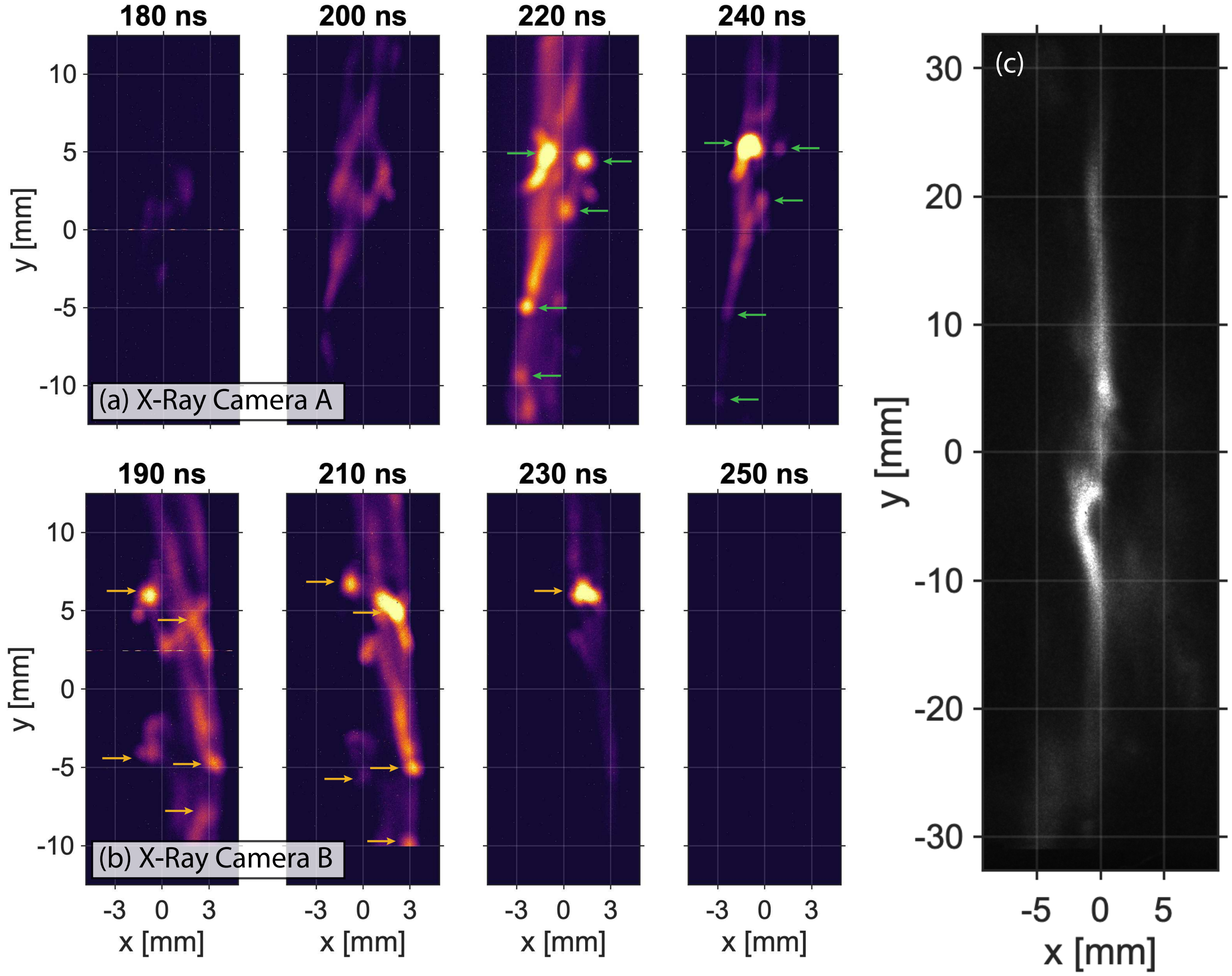

FIG. 8: (a-b) Time-gated X-ray images (10 ns exposure time) of the reconnection layer at between 180-250 ns, recorded using camera A (top row) and camera B (bottom row). X-ray images show brightly emitting hotspots (green and yellow arrows) embedded in an enlonged layer. (c) Time-integrated X-ray image of the reconnection layer. The image was recorded with a 300 µm diameter pinhole, filtered with 2 µm aluminized Mylar.

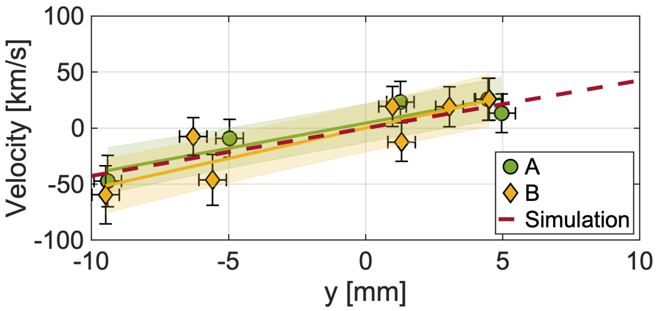

FIG. 9: Hotspot velocity estimated from the translation of the hotspots in the X-ray images of the reconnection layer. Green circles show velocity estimated from Camera A (220-240 ns), while yellow diamonds are for Camera B (190-210 ns). Solid lines show linear fits to the data. Dashed red line is the simulation outflow velocity from the reconnection layer. The uncertainties are determined from the spatial resolution (≈ 1 mm) and the exposure time (10 ns) of the cameras.

which measured > 1 keV X-ray emission (see Figure 7), shows that the spectrum was generated around 220 ± 25 ns.

Lineouts of the recorded spectrum averaged over $z = 10 \pm 0.5$ mm and $z = -10 \pm 0.5$ mm are shown in Figure 10(c-d). We label the Al K-shell emission lines, which include He-like and Li-like satellite transitions. The He-like lines correspond to transitions in Al-XII ions (2 bound electrons, $Z = 11$). Identified He-like lines include the He-α resonance line (1598 eV), the He-α inter-combination (IC) line (1588 eV), and He-α resonance lines with 3p and 3d spectator electrons (1594 eV, 1596 eV). The He-α resonance line ($2p^1P_1 \rightarrow 1s^1S_0$) represents a transition to the ground state $^1S_0$ from the next highest energy state $^1P_1$ of the singlet system, while the intercombination transition ($2p^3P_1 \rightarrow 1s^1S_0$) occurs between the upper term of the triplet system $^3P_1$ and the lower term of the singlet system $^1S_0$.[86,87] The transitions shielded by spectator electrons appear at energies lower than the resonance transition. In the recorded spectra, the He-α resonance and IC lines exhibit roughly similar intensities, while the He-α transitions with spectator electrons have lower intensities.

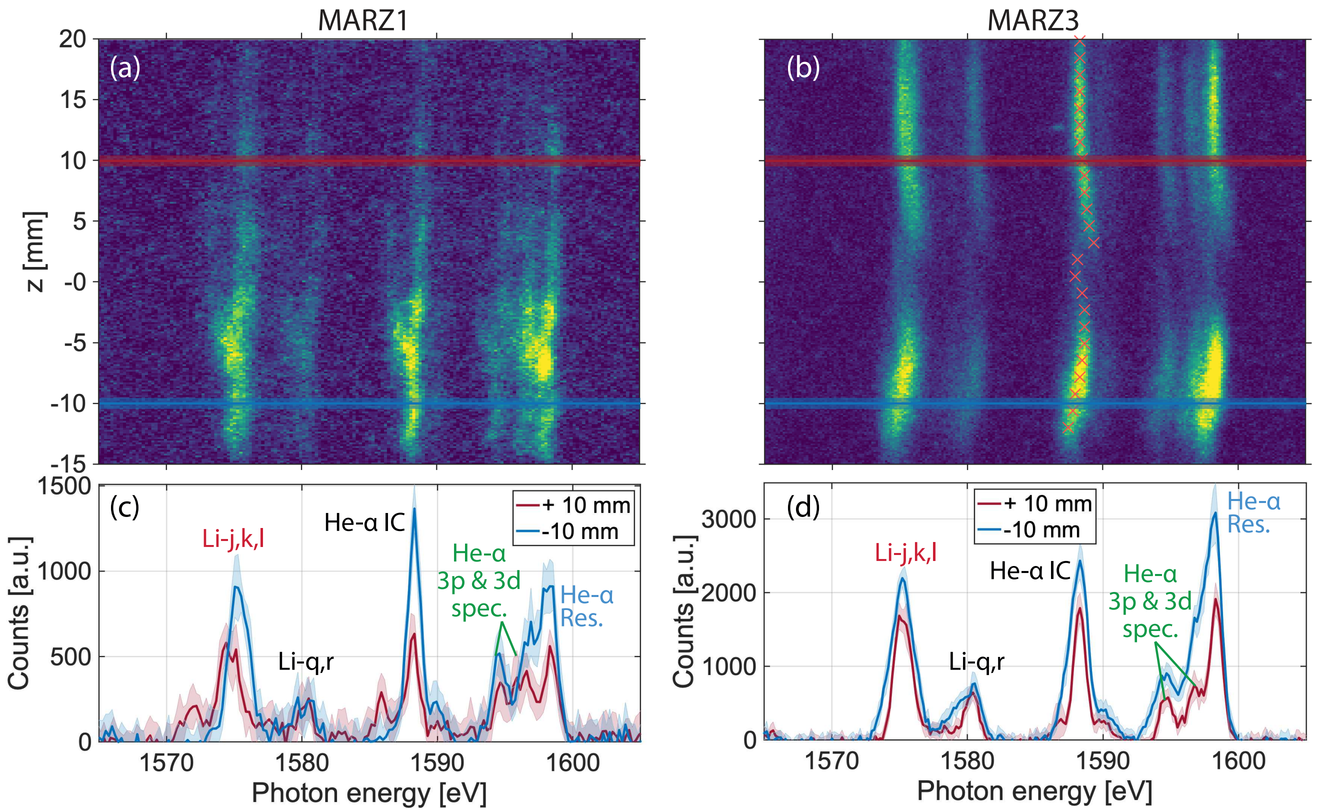

FIG. 10: (a-b) Time-integrated X-ray emission spectra recorded in MARZ1 and MARZ3. (c-d) Lineouts of the X-ray spectra at $z = 10\,\mathrm{mm}$ (red) and $z = -10\,\mathrm{mm}$ (blue), showing Al K-shell emission lines. These include the He-α resonance and inter-combination (IC) lines, the He-α transitions with spectator electrons, and the Li-like satellite transitions. Shaded regions represent the standard deviation of the spectra inside the integration window.

The spectra additionally exhibit Li-like satellite lines. Satellites are transitions from doubly excited states, typically populated via dielectronic recombination.[87] The Li-j (1574.2 eV), Li-k (1575.0 eV), and Li-l (1574.3 eV) lines have similar upper ($1s2p^2$) and lower ($1s^22p^1$) electronic configurations. However, they represent transitions between different combinations of the upper $D_{5/2,3/2}$ and lower $P_{3/2,1/2}$ terms in the doublet system, i.e. these are transitions from upper to lower states with the same orbital angular momentum ($L = 2 \rightarrow L = 1$) but different total angular momentum ($\mathrm{j} : D_{5/2} \rightarrow P_{3/2}, \mathrm{k} : D_{3/2} \rightarrow P_{1/2}, \mathrm{l} : D_{3/2} \rightarrow P_{3/2}$).[86,87] The Li-j,k,l satellites thus have similar energies, and we do not resolve them as separate lines in this experiment. The Li-q (1580.0 eV: $[1s2p2s]\,^2P_{3/2} \rightarrow [1s^22s]\,^2S_{1/2}$) and Li-r (1579.6 eV: $[1s2p2s]\,^2P_{1/2} \rightarrow [1s^22s]\,^2S_{1/2}$) satellites also have similar energies and remain unresolved in Figure 10.

The intensity and spectral position of the recorded lines exhibit modulations along the z-direction. This can be observed in Figure 10, which shows a higher intensity of the lines for $z < 0\,\mathrm{mm}$. In Figure 10b, red crosses indicate the position of He-α IC line; the spectral position varies with z, and the magnitude of this deviation is $< 1\,\mathrm{eV}$. We discuss potential reasons for the observed modulation in a later section.

Although we only show data from MARZ1 and MARZ3 in Figure 10, results from MARZ2 also exhibit the same emission lines, and the line ratios are consistent with that in MARZ1 and MARZ3. In §IV E, we use the line ratios of the observed He-like lines and Li-like satellites to constrain the density, temperature, and homogeneity of the emitting plasma in the reconnection layer.

IV. Discussion of Results

A. Current and Magnetic Field Measurements

In §III A, we observed equal current division of the MITL current between the two wire arrays. In addition, inductive probes measuring the advected magnetic field from separate arrays at the same radial distance (5 mm in MARZ1, 20 mm in MARZ3) recorded similar magnetic field strength, consistent with equal current splitting (Figure 3).

The advected magnetic field, however, does not reproduce the shape of the driving current, but instead exhibits a slower initial rise, followed by a faster ramping up later in time. This happens at around 320 ns for the 5 mm probes in MARZ1 and MARZ3, as seen in Figure 3(b and c). This effect was also observed in simulations of the experiment, and was found to be a consequence of a change in the wire ablation due to heating of the wire cores.[69] In the simulations, the wire cores cool initially, but eventually begin to heat up due to re-absorption of emission generated by the surrounding plasma. The hotter cores are more conductive, and restrict the transport of magnetic field into the plasma flow from the cathode-wire gap. Although this effect is an important consequence of radiation transport observed both in the experiment and simulations,[69] we note that the rise in the magnetic field occurs well after the onset of strong cooling in the experiments (around 220 ns), as discussed later in §IV D.

B. Density and temperature in the inflow region

We estimate the ion density n_i and electron temperature T_e in the inflow to the reconnection layer by performing least-squares-fitting of synthetic spectra to the measured visible spectroscopy data shown in Figure 5(a-d). The synthetic spectra I_ω are generated by solving the steady-state radiation transport equation (Equation 1)[88] along the spectrometer's line-of-sight (LOS) s [see Figure 1], using spectral emissivity $\varepsilon_\omega(n_i, T_e)$ and absorption opacity $\alpha_\omega(n_i, T_e)$ values calculated by PrismSPECT.[89]

$$\partial_s I_\omega(s) = \varepsilon_\omega(s) - \alpha_\omega(s) I_\omega(s) \tag{1}$$

The PrismSPECT model uses a steady-state non-local thermodynamic equilibrium (nLTE) model with Maxwellian free electrons. The PrismSPECT calculations additionally assume a zero-width plasma with no background radiation field; comparison of finite width PrismSPECT simulation results with the zero-width results show that the effect of background radiation is negligible in this regime.[90]

As shown by the green line in Figure 1c, the diagnostic LOS samples plasma ablating from only one array in MARZ1. To solve radiation transport, we assume constant electron temperature along this LOS s. Previous experimental measurements in exploding wire arrays show little spatial variation in the temperature due to high thermal conductivity in pulsed-power-driven plasmas.[91] Because the density falls with radial distance from the wires,[81,82] we expect density along the LOS to peak at the center and fall towards the edges. The rocket model provides a simple description of the variation of mass density generated from wire arrays:[74,92]

$$\rho\left(r,t'\right) = \frac{\mu_0}{8\pi^2 R_0 r V^2}\left[I\left(t' - \frac{r-R_0}{V}\right)\right]^2 \tag{2}$$

Here, r is the radial location around the wire array, $R_0 = 20\,\mathrm{mm}$ is the radius of the wire array, and V is the ablation velocity. A Gaussian function $n_i(s,t) = n_0(t)\exp[(s-s_0)^2/2\sigma(t)^2]$, with peak value $n_0(t)$ and standard deviation $\sigma(t)$ is a good approximation to the expected density along s calculated from Equation 2. Here, s_0 is the center of the diagnostic LOS. Furthermore, using the measured value of the flow velocity $V \approx 110\,\mathrm{km\,s^{-1}}$ (see Figure 4), we constrain the value of $\sigma(t)$ for our analysis, reducing the number of unknowns for fitting.

Figure 11a shows a synthetic fit (orange) to the measured spectrum (black) for the Al-II and Al-III inter-stage lines between 440-480 nm at 220 ± 5 ns, collected at 8 mm from the wires in MARZ1. The synthetic fit reproduces the experimental spectrum well. Ion density is sensitive to the width of the well-isolated Al-II 466 nm line, and electron temperature is sensitive to the line ratio of the inter-stage Al-II 466 nm and Al-III 448 nm and 452 nm lines. Temperature variations modify the relative population densities of the Al-II and Al-III ionization states. Increasing the temperature therefore increases the relative intensity of Al-III lines, while the Al-II lines become weaker, and completely disappear for temperatures $T_e > 4\,\mathrm{eV}$, thus placing an upper bound on the electron temperature.

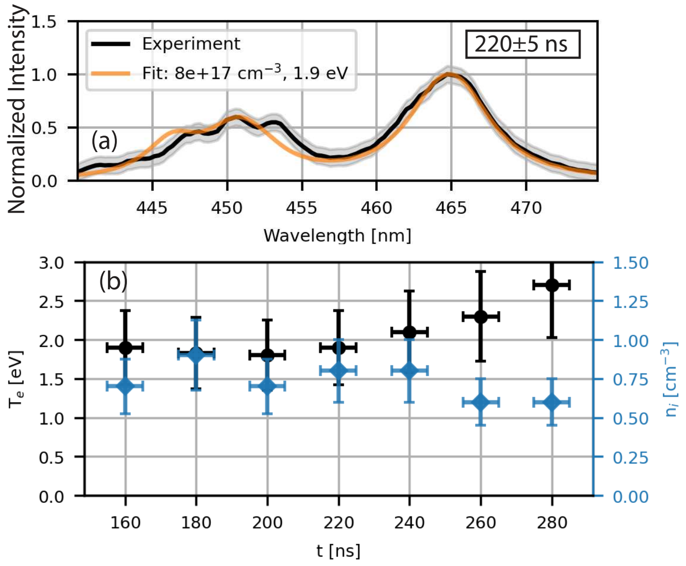

FIG. 11: (a) A least-squares fit of synthetic data (orange) generated from radiation transport and Prismspect simulations to the experimental spectrum (black) at $t = 220 \pm 5$ ns for visible spectra collected at 8 mm from the wires. (b) Temporal variation of electron temperature (black) and ion density (blue) in the inflow region determined by fitting synthetic spectra to the visible spectroscopy data collected at 8 mm from the wires. The error bar in time represents the interval over which the spectra are averaged. The uncertainties in density and temperature are reported to within 25%, based on model error reported in previous literature.[93,94]

The time-resolved ion density and electron temperature determined from this analysis at 8 mm from the wires are shown in Figure 11b. The electron temperature increases from about 1.8 eV at 160 ns to 2.6 eV later in time at 280 ns. The density remains roughly constant, varying between $5-8\times10^{17}\,\mathrm{cm^{-3}}$ between 160-280 ns. After this time, continuum emission dominates, and synthetic spectra indicate that the disappearance of the line emission is consistent with a rise in the ion density $n_i \gtrapprox 3\times10^{18}\,\mathrm{cm^{-3}}$ and temperature $T_e \gtrapprox 3\,\mathrm{eV}$. The increasing density is also consistent with the increasing total emission $\int I(\lambda)d\lambda$ measured at this time in Figure 5a.

Further from the array, at 17 mm from the wires (Figure 5d), the electron temperature is found to be roughly 2 eV between 220-380 ns, and the ion density is lower, at about $2-6\times10^{17}\,\mathrm{cm^{-3}}$ further away from the wires. This shows that the temperature remains roughly constant in the plasma flows, while the density falls with radial distance from the wires, as expected due to divergence.

Finally, we perform synthetic spectral and radiation transport modeling to better understand the absorption features observed in MARZ3 [Figure 5(e-f)], which samples plasma emission and absorption along a chord that includes both arrays and the layer plasma (blue line in Figure 1c). We model the plasma from each array with a Gaussian density (same peak value n_0 and variance σ^2) and a homogeneous temperature T_0. The layer is modeled as a region of thickness 1.5 mm with ion density n_L and temperature T_L. A thickness of 1.5 mm is chosen to match the width of the layer estimated from time-integrated X-ray imaging (§III E 3). A parametric study was performed by varying the layer density and temperature, and the synthetic modeling shows that the layer acts as a continuum backlighter, generating emission that is absorbed by the array plasma between the layer and the collection optics. The synthetic modeling allows us to qualitatively compare the layer density to the array density through inspection of emission and absorption features. When the the layer density n_L is comparable to the peak array plasma density n_0, the higher-opacity Al-II 624 nm line appears as an absorption feature, whereas the other Al lines appear as emission features, which is what is seen in the experiment. For layer densities much greater than the array plasma density, all of the Al lines appear as absorption features, whereas for layer densities less than the array density, all Al lines are emission features. Therefore, the presence of the Al-II 624 nm absorption feature in our experimental spectra [(Figure 5(e-f)] is consistent with the layer density being similar to the array plasma density at this location ($y = 26.5$ mm), which is far away from the center of the layer. Spectra collected further downstream in MARZ3 ($y = 35$ mm) only show emission features and no absorption features, indicating that the layer density decreases as the plasma flows away from the center of the reconnection layer, consistent with resistive MHD simulations of the experiment.[69]

C. Bow Shock Analysis

The measured Mach angle of the bow shock around the T-probe (Figure 6) can provide information about the Mach number in the inflow region. The estimated Mach angle μ of the shock is about $\mu \approx 30^\circ$, which corresponds to an upstream Mach number of about $M_{\text{up}} = 1/\sin(\mu) \approx 2$. The shock stand-off distance, estimated from the width of the emission region at the leading edge of the probe, is about 0.2 mm. The negligible change in the shock structure between 300-400 ns also indicates that the Mach number remains roughly constant.

The resistive diffusion time of the magnetic field through the obstacle and the stagnated plasma is about $\tau_\eta \sim (1\,\text{mm})^2/\bar{\eta}_{\text{glass}} + (0.2\,\text{mm})^2/\bar{\eta}_{\text{plasma}} \sim 0.1 - 1\,\text{ns}$, which is smaller than the hydrodynamic time $L/V \approx 5\,\text{ns}$. Here, we estimate the magnetic diffusivity $\bar{\eta}_{\text{plasma}}$ using Spitzer resistivity calculated with a temperature of $T_e \approx 2 - 10\,\text{eV}$. The flow velocity at this time $V(t = 350\,\text{ns}) \approx 200\,\text{km}\,\text{s}^{-1}$ is determined from the transit time of the plasma to the T-probe. Since the hydrodynamic time is comparable to the diffusion time, decoupling of the magnetic field and the plasma can result in hydrodynamic shock formation.[81,82] From the sonic Mach number $M_S = V/C_S \approx 2$ and the measured flow velocity, we estimate the ion sound speed $C_S \approx \sqrt{\bar{Z}T_e/m_i} \approx 100\,\text{km}\,\text{s}^{-1}$. However, this results in an estimated temperature of $\bar{Z}T_e \approx 2\,\text{keV}$, which is three orders of magnitude larger than the measured temperature in the inflow region from visible spectroscopy.

If, on the other hand, we assume that the shock is magnetohydrodynamic and magnetically dominated $\beta \ll 1$, then $M_A = V/V_A$, and the expected Alfvén speed is $V_A \approx B/\sqrt{\rho\mu_0} \approx 100\,\text{km}\,\text{s}^{-1}$. In §IV F, we show that the plasma $\beta \approx 0.1$ in the inflow region. From the measured value of the magnetic field ($B \approx 3$ T) at this time, the estimated ion density from the shock shape is $2 \times 10^{16}\,\text{cm}^{-3}$, which is an order of magnitude lower than the expected density inferred from visible spectroscopy. We note that this is an upper bound on the density estimate from the shock shape, because the probe would measure a higher compressed magnetic field for MHD shock formation.

Therefore, the observed shock shape does not match the inflow conditions measured using inductive probes and visible spectroscopy. A potential cause of this discrepancy could be the generation of photo-ionized plasma from the probe surface, because of the harsh X-ray environment provided by the Z machine. Photo-ionized plasma at the T-probe tip may increase the post-shock pressure, creating a larger shock angle. Further investigation of this mismatch will require direct measurements of the post-shock density and temperature, and will be pursued in future experiments.

D. Radiative Cooling and Generation of High-Energy Emission from the Reconnection Layer

The X-ray diode signals (Figure 7) and the X-ray cameras (Figure 8) both show a transient burst of high-energy X-ray emission from the reconnection layer. The initial rise in X-ray emission is consistent with increasing density and/or temperature of the reconnection layer during the formation stage. The temperature in the layer is initially high enough to generate high-energy X-rays with energies $> 1\,\text{keV}$. The subsequent fall in X-ray emission after 220 ns is consistent with rapid radiative cooling of the layer. The temporal change of X-ray intensity measured by the diodes also matches the intensity evolution observed in the X-ray images (Figure 8).

We also observe a sharp fall in X-ray emission from the reconnection layer in radiative resistive MHD simulations of the MARZ experiment.[69] In the simulations, radiative collapse of the current sheet, characterized by a sharp fall in the layer temperature and a simultaneous rise in density, begins around 200 ns after current start. In Figure 12a, we plot synthetic diagnostic data, calculated from simulations, of the filtered X-ray emission generated from the reconnection layer as a function of time. The filtered X-ray emission is generated by post-processing the simulation results using radiation transport modeling in XP2.[69] We spatially integrate the output intensity, and filter it using transmission curves for both 8 µm Be and 2 µm Mylar, in order to match the diode filters in the experiment. In Figure 12a, we additionally show the expected X-ray emission (filtered with 8 µm Be) for the case with no radiative cooling.

In the absence of radiative cooling, X-ray emission from the layer would continue to rise, as the layer density ramps up in time at a consistently high temperature $> 100\,\text{eV}$. In the radiatively-cooled case, however, the emission peaks and then falls sharply, similar to that in the experiment. The temperature in the layer is initially $> 100\,\text{eV}$, which is high enough to generate $> 1\,\text{keV}$ X-rays. However, the subsequent fall in X-ray emission occurs due to radiative collapse of the layer, which rapidly cools as the density increases. The simulations therefore confirm that the rapid fall in X-ray emission is an experimental signature for strong radiative cooling of the reconnection layer. Figure 12a also shows that the FWHM of the harder ($> 1\,\mathrm{keV}$) emission is shorter than that of softer $> 100\,\mathrm{eV}$ emission, similar to that in the experiment. This is expected, since as the temperature of the emitting plasma falls, the spectral distribution of the emitted radiation shifts to lower energies. Thus, the higher-energy emission falls earlier than the lower-energy emission.

Simultaneous measurements of X-ray emission by the $8\,\mu\mathrm{m}$ Be and $2\,\mu\mathrm{m}$ Mylar filtered diodes in the experiment (Figure 7) provide constraints on the temperature of the emitting plasma. Figure 12c shows the emissivity of an aluminum plasma with ion density $5 \times 10^{18}\,\mathrm{cm}^{-3}$ as a function of the plasma temperature, calculated using the atomic code Spk.[95] Spk uses a nLTE model and includes line, recombination, and bremsstrahlung emission.[69] The unfiltered emissivity exhibits a smaller peak around $T \approx 50\,\mathrm{eV}$; the emissivity is lower between 50-100 eV, and increases for $T > 100\,\mathrm{eV}$. The smaller peak results from L-shell line emission of photons with energies of $100-300\,\mathrm{eV}$, while the increased emission at temperatures $T > 100\,\mathrm{eV}$ is due to higher energy $> 1\,\mathrm{keV}$ Al K-shell emission. We also show the emissivity filtered using X-ray transmission tables for $8\,\mu\mathrm{m}$ Be and $2\,\mu\mathrm{m}$ Mylar in Figure 12c. The $8\,\mu\mathrm{m}$ Be filter significantly attenuates radiation with energies $< 1\,\mathrm{keV}$, whereas the $2\,\mu\mathrm{m}$ Mylar filter exhibits a smaller window of transmission around photon energies $\approx 200\,\mathrm{eV}$. Therefore, the filtered emissivity through $2\,\mu\mathrm{m}$ Mylar is significant for temperatures $T > 25\,\mathrm{eV}$, while for $8\,\mu\mathrm{m}$ Be the signal is only significant for temperatures $T > 100\,\mathrm{eV}$.[96]

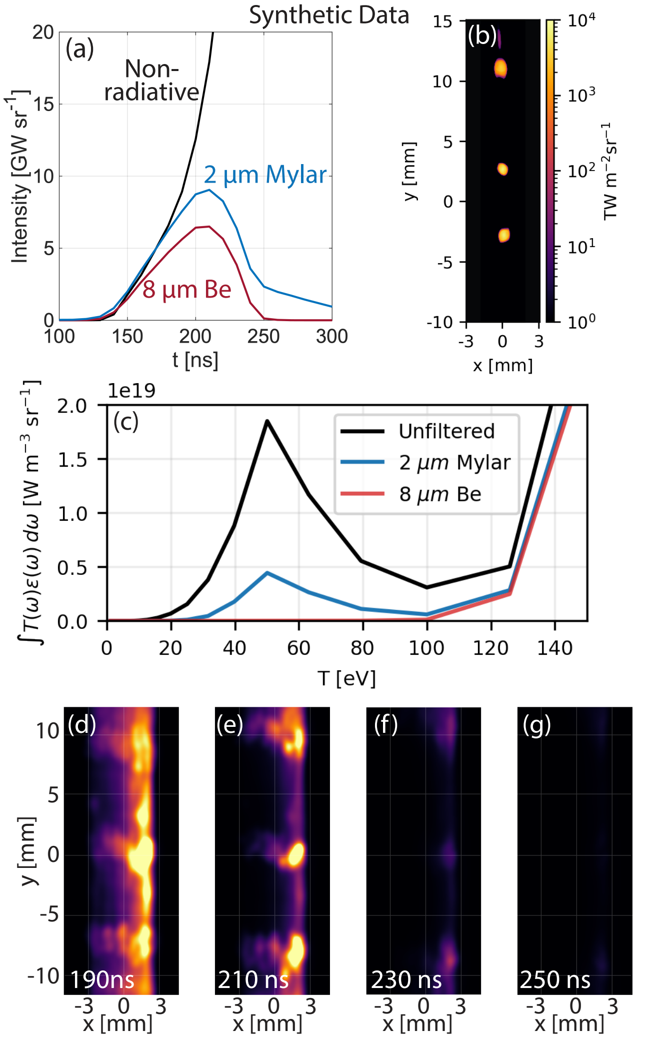

FIG. 12: Synthetic diagnostics from simulations of the MARZ experiment: (a) Filtered X-ray emission from the reconnection layer. The emission is filtered with $8\,\mu\mathrm{m}$ Be (red) and $2\,\mu\mathrm{m}$ Mylar (blue) to match the diode filters in the experiment. The black curve shows the expected X-ray emission (filtered with $8\,\mu\mathrm{m}$ Be) for the simulation with no radiative cooling. (b) X-ray emission from the layer filtered with $8\,\mu\mathrm{m}$ Be. Plasmoids primarily generate high-energy $> 1\,\mathrm{keV}$ emission from the layer. (c) Filtered emissivity of the aluminum plasma generated using Spk tables. (d-g) Synthetic X-ray images of the reconnection layer, filtered with $2\,\mu\mathrm{m}$ Mylar, and using the same line of sight as X-ray camera B in Figure 8. X-ray emission from the layer decreases with time due to radiative cooling.

The different responses of the filtered diodes shown in Figure 12c allows us to constrain the temperature of the emitting plasma. Initially, in region A (see Figure 7), where neither diode records any signal, we expect the plasma temperature to be $T < 25\,\mathrm{eV}$. In region B, where the Mylar diode records signal, while the Be diode does not, the temperature of the emitting plasma is constrained to be $25 < T < 100\,\mathrm{eV}$. In C, where both diodes simultaneously record signals, the temperature must be $T > 100\,\mathrm{eV}$. Similarly, the expected temperature is $25 < T < 100\,\mathrm{eV}$, and $T < 25\,\mathrm{eV}$ in regions D and E respectively. Therefore, the diode signals indicate an initial heating of the reconnection layer to temperatures $> 100\,\mathrm{eV}$, followed by a sharp fall below $T < 25\,\mathrm{eV}$ due to radiative cooling. We show later that the expected temperature at the time of peak emission (region C), is consistent with results from X-ray spectroscopy analysis in §IV E.

The diodes collect time-resolved emission integrated over the entire reconnection layer. The time-gated X-ray images (Figure 8) complement this measurement by providing spatial resolution at discrete times. These images were also filtered with $2\,\mu\mathrm{m}$ Mylar, and at around 190-200 ns both the layer and hotspots generate emission in the spectral range transmitted by the Mylar filter, indicating both the hotspots and the layer have $T > 25\,\mathrm{eV}$. Later in time (230-240 ns), the hotspots remain bright, while emission from the layer has significantly decreased. This indicates that the layer has cooled to $T < 25\,\mathrm{eV}$, while the hotspots have remained above 25 eV, such that the signal on the Mylar filtered diode is dominated by hotspot emission. By 250 ns, there is no emission recorded on the X-ray camera or the Mylar filtered diode, consistent with both the hotspots and the layer cooling to $T < 25\,\mathrm{eV}$.

Figure 12(d-g) show synthetic X-ray images of the reconnection layer generated from post-processing the 3D simulation results in XP2 between 190-250 ns. The synthetic images are filtered with $2\,\mu\mathrm{m}$ Mylar, and use the same LOS as X-ray camera B in the experiment (see Figure 1d). As observed in Figure 12(d-g), emission from the reconnection layer falls as a result of radiative cooling, consistent with the experimental images in Figure 8. The synthetic images also show hotspots of emission within the elongated reconnection layer, similar to that in the experiment. These hotspots correspond to the position of magnetic islands or plasmoids in the simulations, which are generated by the tearing instability.[47,97] The plasmoids appear as localized regions of enhanced emission due to their relatively higher electron density and temperature.[69] Enhanced emission from plasmoids has also been reported in relativistic-PIC simulations of extreme astrophysical objects.[35]

The majority of the high-energy emission is generated by the plasmoids in our simulations because of their higher temperature. This can be observed in Figure 12b, which shows X-ray emission from the reconnection layer filtered with 8 µm Be. Emission recorded by the 8 µm Be filtered diode in the experiment may thus be dominated by higher energy emission from the hotspots with temperature $T > 100\,\mathrm{eV}$. This is further supported by the analysis of X-ray spectroscopy from the experiment, which is provided in the following subsection.

E. Analysis of X-Ray Spectroscopy

We estimate the temperature and density of the plasma in the reconnection layer by comparing the measured spectra shown in Figure 10 with synthetic spectra. We use the atomic code SCRAM to generate nLTE spectral emissivity $\varepsilon_\omega(n_i, T_e)$ and absorption opacity $\alpha_\omega(n_i, T_e)$ tables,[98] which are then used to solve the radiation transport equation[88] (Equation 1) along the diagnostic LOS to model the output intensity spectrum. For this analysis, SCRAM includes spectral line broadening effects (Stark and thermal Doppler), and incorporates a background radiation field by assuming a homogeneous cylindrical plasma of diameter 1 mm. A characteristic length of 1 mm is chosen because it is comparable to the width of the X-ray emission region, as observed in X-ray images of the reconnection layer (Figure 8, Figure 8c). The contribution of scattering to the total opacity is expected to be small in this regime, and is thus, excluded from the SCRAM calculations.

The SCRAM results show that Al K-shell lines do not appear for temperatures below 60 eV. Furthermore, as expected for inter-stage transitions,[87] the relative emissivities of the Li-like satellites and He-like lines are strong functions of temperature. Li-like satellites exhibit higher emissivities at lower temperatures, whereas the emissivity of He-like lines dominates at higher temperatures. The He-α resonance transition exhibits much higher emissivities and opacities compared to the other He-like lines, consistent with the relatively higher probability of the resonance transition.[86,87] At $T_e \approx 100\,\mathrm{eV}$, the Li-j,k,l satellites and the He-α resonance line have similar emissivity values; however, the opacity of the He-α resonance line is several orders of magnitude higher than both the Li-like satellites and other He-like lines. For instance, at $n_i = 1\times10^{18}\,\mathrm{cm}^{-3}$ and $T_e = 100\,\mathrm{eV}$, the attenuation length scale α_ω^{-1} for the He-α resonance line is about 0.1 mm, while that for the other He-like lines and Li-like satellites is $> 10\,\mathrm{mm}$. Therefore, due to the high opacity of the He-α resonance line, radiation transport calculations are required to accurately model the spectral intensity of the emission from the reconnection layer.

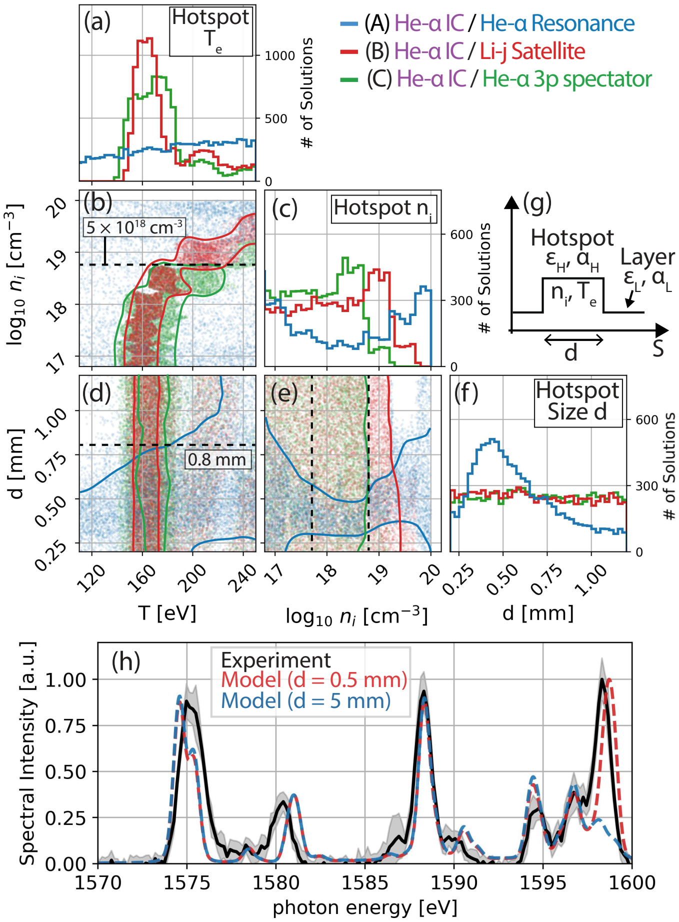

FIG. 13: Corner plot of solutions which match the line ratios of (A) He-α IC / He-α Resonance (blue), (B) He-α IC / Li-j Satellite (red), and (C) He-α IC / He-α with 3p spectator (green). (b, d, and e) show the 2D scatter plots for n_i, T_e, and d; (a, c, and f) show the probability density distributions of these values for valid solutions. Solid lines represent contours enclosing 90% of the solutions. (g) Radiation transport model for emission from a single hotspot with emissivity ε_H and opacity α_H, embedded in a homogeneous layer with ε_L and opacity α_L. (h) Comparison of synthetic spectra with the experimental spectrum ($z = 10\,\mathrm{mm}$, MARZ3). Both synthetic spectra are calculated for $T = 170\,\mathrm{eV}$ and $n_i = 1\times10^{18}\,\mathrm{cm}^{-3}$, but using sizes of $d = 0.5\,\mathrm{mm}$ (red) and $d = 5\,\mathrm{mm}$ (blue) respectively.

To solve the 1D radiation transport problem along the diagnostic LOS, we first assume emission from a plasma of length d with homogeneous ion density n_i and electron temperature T. Values of n_i, T, and d are then randomly sampled from uniform distributions to find solutions that match within 20% the experimentally observed line ratios. The model includes the effect of source and instrument broadening, but neglects Doppler shift, which is $< 0.25\,\mathrm{eV}$, as calculated from the hotspot velocities in Figure 9. In particular, we compare three different line ratios shown in Figure 10d — (A) He-α IC / He-α Resonance (blue), (B) He-α IC / Li-j Satellite (red), and (C) He-α IC / He-α with 3p spectator (green). Figure 13 shows a corner plot of the solutions that individually satisfy these line ratios at $z = 10\,\mathrm{mm}$ in MARZ3 (see Figure 10d). The corner plot shows one and two-dimensional projections of the three-dimensional parameter space —–Figure 13(b, d, and e) are 2D scatter plots for solutions, while Figure 13(a,c and f) show the probability distribution functions for the values of n_i, T and d of the solutions. The solid contours in Figure 13(b, d, and e) enclose 90% of the solutions. The intersection of the solutions for these line ratios constrains the properties of the emitting plasma.

As seen in Figure 13b, which shows a scatter plot of the ion density against temperature, solutions for the B (red) and C (green) line ratios constrain T_e to a narrow band around $T \approx 170 \pm 20\,\mathrm{eV}$, and provide an upper bound of about $n_i \lesssim 5 \times 10^{18}\,\mathrm{cm}^{-3}$ on the ion density (indicated via the black dashed line). These bounds are determined from the intersection of these solutions. The size of the plasma d is poorly constrained from these line ratios, since line ratios B and C are for the optically thin lines, and optical depth $(\alpha_\omega(n_i, T_e)d)$ thus has a limited effect. Figure 13(d and e) also clearly show overlapping solutions at $T \approx 170 \pm 20\,\mathrm{eV}$ and $n_i \lesssim 5 \times 10^{18}\,\mathrm{cm}^{-3}$ respectively, but exhibit a wide range of possible values for d.

The size of the emitting plasma can, however, be constrained through solutions for line ratio A (blue). Line ratio A is the relative intensity of the He-α IC compared to the higher opacity He-α resonance line, which is a strong function of optical depth. This line ratio is well satisfied for a wide range of T, n_i and d; however, from Figure 13d, we observe that for temperatures $T = 170 \pm 20\,\mathrm{eV}$ that satisfy line ratios B and C, line ratio A is only satisfied for $d \leq 0.8\,\mathrm{mm}$ (indicated via the black dashed line). If the size of the emitting plasma exceeds this value, we can no longer satisfy all line ratios simultaneously because of over-damping of the high-opacity He-α resonance line. Notably this value for d is significantly lower than the length of the reconnection layer observed in Figure 8c, which implies that only a small region of the layer is contributing to the the emissivity and opacity of the system for these photon energies.

This is further illustrated in Figure 13h, which compares two synthetic spectra to the experimental spectrum at $z = 10\,\mathrm{mm}$ (MARZ3). Both synthetic spectra are calculated for $T = 170\,\mathrm{eV}$ and $n_i = 1 \times 10^{18}\,\mathrm{cm}^{-3}$, but using sizes of $d = 0.5\,\mathrm{mm}$ (red) and $d = 5\,\mathrm{mm}$ (blue) respectively. As expected, the synthetic spectrum for $d = 0.5\,\mathrm{mm}$ reproduces the line ratios and line widths of the experimental spectrum well. The synthetic spectrum for $d = 5\,\mathrm{mm}$ reproduces the relative intensities of the Li-like satellites and the He-α IC and spectator transitions, but fails to reproduce the He-α resonance line. This analysis therefore indicates that Al K-shell emission from the reconnection layer is predominantly generated by sub-millimeter size hotspots in the layer. This is further supported by the X-ray images of the layer (Figure 8) that show the presence of strongly-emitting hotspots of size $< 1\,\mathrm{mm}$, as well as by the simulations, which show strong localized emission of $> 1\,\mathrm{keV}$ photons from the plasmoids (Figure 12b). Assuming that the hotspot density lies between the upper bound of $n_i \leq 5 \times 10^{18}\,\mathrm{cm}^{-3}$ and the lower bound of $n_i \geq 5 \times 10^{17}\,\mathrm{cm}^{-3}$, which is the inflow density from visible spectroscopy (Figure 11), we find, from Figure 13e, that $0.3 \leq d \leq 0.5\,\mathrm{mm}$, consistent with the plasmoid widths observed in simulations.[69]

The maximum temperature achievable due to the thermalization of the plasma kinetic energy by shock heating is only about $T_{max} = [(m_i V_{in}^2)/2]/(\bar{Z}+1)(\gamma-1)/(\gamma+1)^2 \approx 50\,\mathrm{eV}$.[67] The temperature of the hotspots measured from X-ray spectroscopy $T_e \approx 170\,\mathrm{eV}$ is larger than this value, thus showing that shock compression cannot account for the heating observed in the experiment.

To estimate an upper bound on the bulk temperature of the layer, we consider a simple model that includes a single hotspot of size d embedded in a homogeneous layer with emissivity ε_L and opacity α_L, as shown in Figure 13g. Radiation transport solutions for this model indicate that the bulk layer temperature must be less than about $T_{\mathrm{bulk}} \leq 75\,\mathrm{eV}$. At around $T_{\mathrm{bulk}} \approx 75\,\mathrm{eV}$, contribution from the layer is not negligible and modifies the spectral intensity from the hotspots; however, solutions that satisfy the line ratios in the experiment are still possible. At higher layer temperatures, the He-α resonance line becomes strongly absorbed by the layer, and the experimental spectrum can no longer be reproduced.

Figure 10 shows that the hotspots form elongated structures of length $\sim 10\,\mathrm{mm}$ along z. The above analysis was repeated at multiple z-positions for the different shots. Although bounds on the inferred hotspot density, temperature, and size show slight variations along z, the values remain largely consistent. This is unsurprising because the same Al K-shell lines are observed at different z and the line ratios remain largely similar, despite small modulations, as seen in Figure 10. The modulation in the spectral position of the lines is unlikely to be caused by Doppler shift — as mentioned before, the maximum Doppler shift expected is 0.25 eV, which is smaller than the 1 eV modulation seen in Figure 10. The spectral modulations could be a result of modulations in the position of the hotspots in the object plane along x. Deviations in the source position can lead to deviations in the position of the lines recorded on the image plate. From ray tracing simulations,[85] the observed deviation in spectral position corresponds to a roughly 1 mm deviation in the position of the hotspots. This deviation is comparable to the amplitude of the modulations in the plasmoid position generated by the MHD kink instability in the 3D simulation of the experiment.[69] Thus, the spectral deviation of the lines along z may be a preliminary indication of the MHD kink instability of the plasmoids.

F. Cooling Rate

Our analysis of the experimental data in the previous sections has provided quantitative estimates of the plasma properties. In this section, we use these experimental results to further characterize the net cooling rate in the reconnection layer at the time of peak X-ray emission ($t = 220\,\mathrm{ns}$, see Figure 7).

The temporal evolution of the reconnection layer temperature depends on the relative magnitudes of the terms in the internal energy equation:[99]

$$\frac{\partial}{\partial t}(\rho\varepsilon) + \nabla\cdot(\rho\varepsilon\mathbf{v}) = \eta|j|^2 - p\nabla\cdot\mathbf{v} + \nabla\mathbf{v} : \tau - P_{rad} \quad (3)$$

Here, $\rho\varepsilon = p/(\gamma-1)$ is the internal energy density, $\nabla\cdot(\rho\varepsilon\mathbf{v})$ is the advective term, $\eta|j|^2$, $-p\nabla\cdot\mathbf{v}$, and $\nabla\mathbf{v} : \tau$ are the compressional, resistive, and viscous heating terms respectively. Lastly, P_{rad} is the volumetric radiative loss from the layer. We estimate the order-of-magnitude of these terms

TABLE I: Estimated magnitudes of terms in the energy equation for the reconnection layer

Term	Estimate	Value [$\mathrm{W\,m^{-3}}$]
$\eta\|j\|^2$	$\eta\,(B_{in}/\mu_0\delta_{SP})^2$	2×10^{15}
$-p\nabla\cdot\mathbf{v}$	$p_L(V_{in}/\delta_{SP}-V_{out}/L)$	6×10^{15}
$\nabla\mathbf{v}:\tau$	$\mu(V_{in}/\delta_{SP})^2$	1×10^{9}
$\nabla\cdot(\rho\varepsilon\mathbf{v})$	$(p_{in}V_{in}/\delta_{SP}-p_LV_{out}/L)/(\gamma-1)$	3×10^{15}
P_{rad}	Equation 4	1×10^{18}

based on the plasma parameters in the layer and in the inflow, as shown in the second column of Table I. Here, B_{in}, p_{in} and V_{in} are the magnetic field, thermal pressure, and velocity in the inflow just outside the layer, and p_L and V_{out} are the layer pressure and the reconnection outflow velocity. The half-length and the half-width of the layer are denoted by L and δ respectively. Lastly, η and μ are the (Spitzer) resistivity and plasma viscosity,[100] while γ is the adiabatic index.[88]

To determine the net cooling rate, we require estimates of the inflow and layer parameters listed above. In our previous paper, Ref. 73, we presented approximations of these parameters at 220 ns, in addition to other key parameters such as the reconnection rate $V_{in}/V_{out}\approx0.3$, the Lundquist number $S_L\approx120$, and the Sweet-Parker layer width $\delta_{SP}\approx1.4\,\mathrm{mm}$. A detailed discussion of how these parameters are estimated from the experimentally measured quantities is provided in Appendix A.

Using the quantities listed in Table II (Appendix A), we now estimate the relative magnitudes of the terms in the energy equation (see Table I). As observed in the third column of Table I, Ohmic heating, compressional heating, and net enthalpy advection into the layer, are estimated to have similar magnitudes, whereas the contribution of viscous heating is small. The Ohmic dissipation rate $\eta j^2\sim2\times10^{15}\,\mathrm{W\,m^{-3}}$ is roughly half the estimated magnetic energy injection rate per unit volume into the layer $(B_{in}^2/\mu_0)V_{in}/(2\delta_{SP})\sim5\times10^{15}\,\mathrm{W\,m^{-3}}$. We also note that comparing the conductive heat flux $-\kappa\nabla T\sim\kappa(T_L-T_{in})/\delta_{SP}$ with the advective flux $p_{in}V_{in}/(\gamma-1)$ along the $x-$direction shows that conduction losses from the layer to the upstream inflow are expected to be small ($q_{cond,x}/q_{adv,x}<0.1$). Here, κ is the parallel thermal conductivity in the layer, which is a function of the layer density and temperature T_L,[100] and T_{in} is the inflow temperature.

We estimate the radiative loss rate P_{rad} from the layer by solving the radiation transport equation (Equation 1) for an isotropically emitting and absorbing medium.[69,95]

$$P_{\mathrm{rad}}=\frac{3}{4R}\int\frac{4\pi\varepsilon_\omega}{\alpha_\omega}\left[1+\frac{2}{\tau_\omega^2}\left\{(1+\tau_\omega)e^{-\tau_\omega}-1\right\}\right]d\omega \quad (4)$$

Here, ε_ω and α_ω are the spectral emissivities and opacities respectively, and $\tau_\omega=2\alpha_\omega R$ is the optical depth. R is the characteristic distance traveled by the radiation leaving the reconnection layer, which we approximate using the volume-to-surface area ratio $R=(1/\delta_{SP}+2/L)^{-1}$ of a cuboidal slab of width $2\delta_{SP}$, and height and length $2L$. Spectral emissivity and opacity values for the estimated layer temperature and density are determined from SpK.[72] The radiative loss rate calculated using Equation 4 is $P_{\mathrm{rad}}\sim10^{18}\,\mathrm{W\,m^{-3}}$, which is significantly larger than the total heating rate $P_{heat}\sim10^{16}\,\mathrm{W\,m^{-3}}$, calculated from the sum of the Ohmic, compressional, viscous, and enthalpic terms provided in Table I. The dimensionless cooling parameter is $R_{\mathrm{cool}}\equiv\tau_{\mathrm{cool}}^{-1}/\tau_A^{-1}\approx50$ at 220 ns. Here, $\tau_{\mathrm{cool}}=p_L/[(\gamma-1)(P_{rad}-P_{heat})]\approx6\,\mathrm{ns}$ and $\tau_A=L/V_{A,in}\approx300\,\mathrm{ns}$ are the net cooling and Alfvén transit times respectively. We thus expect the plasma to cool before being ejected out of the layer, which is consistent with the strong cooling inferred from the X-ray diagnostics of the reconnection layer (see §IV D).

A similar analysis can be used to estimate the cooling time for the hotspots, which are at a a higher temperature of $T_{\mathrm{hotspot}}\approx170\,\mathrm{eV}$. The radiative cooling rate estimated from Equation 4 is about $P_{\mathrm{rad,hotspot}}\sim10^{19}\,\mathrm{W\,m^{-3}}$, roughly an order of magnitude higher than that in the rest of the layer. The radiative cooling time $\tau_{\mathrm{cool}}=p_{\mathrm{hotspot}}/(\gamma-1)/P_{\mathrm{rad,hotspot}}\approx2\,\mathrm{ns}$. We note that in calculating this cooling time, we have not included the heating rate, therefore this value represents a lower bound on the cooling time. As mentioned in §IV D, we reiterate that cooling of the hotspots, which are at a higher temperature at this time, is primarily due to high-energy (> 1 keV) X-rays, while that for the rest of the layer, which is colder, is dominated by softer X-rays. In future experiments, we aim to use time-resolved density and temperature measurements to characterize how the estimated cooling time compares to the time-evolution of the hotspot and layer properties.

V. Conclusions

We present results from a strongly-radiatively cooled pulsed-power-driven magnetic reconnection experiment. Unlike previous pulsed-power-driven experiments, which either achieved strong cooling without plasmoid formation at low Lundquist numbers ($S_L<10$),[62,67] or insignificant cooling with plasmoid formation at higher Lundquist numbers ($S_L\sim100$),[63,65] here we simultaneously achieve strong cooling $R_{\mathrm{cool}}\gg1$ and plasmoid formation at $S_L>100$. Using a suite of current, inflow, and reconnection layer diagnostics, as described in §II B, we obtain the following key results: (1) X-ray emission from the reconnection layer, as measured by the X-ray diodes and time-gated X-ray cameras, rises initially and then falls sharply, consistent with rapid cooling of the layer (see §IV D). A similar effect is seen in radiative resistive magnetohydrodynamic simulations of the experiment, which show that X-ray emission would simply continue to rise without radiative cooling.[69] (2) The reconnection layer exhibits sub-millimeter size localized regions of strong X-ray emission (see §III E 2). These hotspots are consistent with the presence of plasmoids generated by the tearing instability in our simulations,[69] which generate strong X-ray emission due to their higher electron density and temperature compared to the rest of the layer. (3) These hotspots generate the majority of the high-energy X-ray emission from the layer; this is supported by X-ray images of the layer, and by X-ray spectroscopy, which shows that the measured X-ray spectra can be best explained by emitting regions of size < 1 mm (see §IV E). The generation of high-energy emission predominantly from the plasmoids is also observed in the simulations, as shown in

Figure 12.

Using the measured quantities, we infer key physical and dimensionless parameters describing the plasma in the inflow region and the reconnection layer in §IV F. The estimated values of layer density, temperature, and size are consistent with bounds determined from experimental diagnostics. Finally, using these inferred quantities, we compare the various terms in the energy equation (Table I), and show that radiative loss is expected to dominate the total heating rate inside the reconnection layer ($R_{\text{cool}} \sim 50$). This further supports the strong cooling observed in the experiment.

Strong radiative cooling is expected to result in radiative collapse of the current sheet, similar to that in the simulations.[75] In future experiments, we will further characterize the collapse of the reconnection layer at later times using time-resolved measurements of the density, size, and compression of the layer. Our current experiments additionally provide preliminary evidence of the 3D modulations in the structure of the plasmoids, and future experiments will further probe this 3D structure using time-resolved laser imaging.

The results in this paper provide insight into a regime of magnetic reconnection that has not been previously explored in laboratory experiments. Our detailed measurements of the entire reconnection process provide high-quality data for benchmarking atomic codes and radiative-magnetohydrodynamic simulations. Our findings on the generation of transient X-rays bursts from the layer, and the localization of the high-energy emission within the plasmoids, are relevant to understanding observations of reconnection in remote and extreme astrophysical environments. Finally, the MARZ platform exhibits rich radiative physics, allowing for the investigation of radiation transport and cooling effects in HED plasmas beyond their relevance to magnetic reconnection.

VI. Acknowledgements

The authors would like to thank the Z machine operations teams and the target fabrication team for their contributions to this work. Experimental time on the Z facility was provided through the Z Fundamental Science Program. This work was funded by NSF and NNSA under grant no. PHY2108050, by the EAGER grant no. PHY2213898. RD acknowledges support from the MIT MathWorks and the MIT College of Engineering Exponent fellowships. DAU gratefully acknowledges support from NASA grants 80NSSC20K0545 and 80NSSC22K0828. This work was supported by Sandia National Laboratories, a multimission laboratory managed and operated by the National Technology and Engineering Solutions of Sandia, LLC, a wholly owned subsidiary of Honeywell International, Inc., for the U.S. Department of Energy's National Nuclear Security Administration under Contract No. DE-NA0003525. This paper describes objective technical results and analysis. Any subjective views or opinions that might be expressed in the paper do not necessarily represent the views of the U.S. Department of Energy or the United States Government.

VII. Declaration of Conflicts of Interest

The authors have no conflicts of interest to disclose.

VIII. Data Availability

The data that support the findings of this study are available from the corresponding author upon reasonable request.

[1] E. N. Parker, "The solar-flare phenomenon and the theory of reconnection and annihiliation of magnetic fields." ApJ. Supplement Series **8**, 177 (1963).

[2] S. Masuda, T. Kosugi, H. Hara, S. Tsuneta, and Y. Ogawara, "A loop-top hard x-ray source in a compact solar flare as evidence for magnetic reconnection," Nature **371**, 495 (1994).

[3] M. Yamada, R. Kulsrud, and H. Ji, "Magnetic reconnection," Rev. Mod. Phys. **82**, 603 (2010).

[4] A. P. Goodson, R. M. Winglee, and K.-H. Böhm, "Time-dependent accretion by magnetic young stellar objects as a launching mechanism for stellar jets," ApJ **489**, 199 (1997).

[5] E. D. Feigelson and T. Montmerle, "High-energy processes in young stellar objects," Annual Review of Astronomy and Astrophysics **37**, 363–408 (1999).

[6] A. O. Benz and M. Güdel, "Physical processes in magnetically driven flares on the sun, stars, and young stellar objects," Annual Review of Astronomy and Astrophysics **48**, 241–287 (2010).

[7] E. G. Zweibel, "Magnetic reconnection in partially ionized gases," ApJ **340**, 550–557 (1989).

[8] A. Brandenburg and E. G. Zweibel, "Effects of pressure and resistivity on the ambipolar diffusion singularity: too little, too late," ApJ **448**, 734 (1995).

[9] A. Lazarian and E. T. Vishniac, "Reconnection in a weakly stochastic field," ApJ **517**, 700 (1999).

[10] F. Heitsch and E. G. Zweibel, "Fast reconnection in a two-stage process," ApJ **583**, 229 (2003).

[11] E. N. Parker, "Sweet's mechanism for merging magnetic fields in conducting fluids," J. Geophys. Res. **62**, 509 (1957).

[12] H. Ji, W. Daughton, J. Jara-Almonte, A. Le, A. Stanier, and J. Yoo, "Magnetic reconnection in the era of exascale computing and multiscale experiments," Nature Reviews Physics **4**, 263–282 (2022).

[13] B. V. Somov and S. I. Syrovatski, "Physical processes in the solar atmosphere associated with flares," Soviet Physics Uspekhi **19**, 813 (1976).

[14] D. A. Uzdensky, "Magnetic reconnection in extreme astrophysical environments," Space Sci. Rev. **160**, 45 (2011).

[15] D. A. Uzdensky, "Radiative magnetic reconnection in astrophysics," in *Magnetic reconnection* (Springer, 2016) p. 473.

[16] J. Goodman and D. Uzdensky, "Reconnection in marginally collisionless accretion disk coronae," ApJ **688**, 555 (2008).

[17] A. M. Beloborodov, "Radiative magnetic reconnection near accreting black holes," ApJ **850**, 141 (2017).

[18] G. R. Werner, A. A. Philippov, and D. A. Uzdensky, "Particle acceleration in relativistic magnetic reconnection with strong inverse-compton cooling in pair plasmas," Monthly Notices of the Royal Astronomical Society: Letters **482**, L60–L64 (2019).

[19] B. Ripperda, F. Bacchini, and A. A. Philippov, "Magnetic reconnection and hot spot formation in black hole accretion disks," ApJ. **900**, 100 (2020).

[20] M. Lyutikov, "The electromagnetic model of gamma-ray bursts," New Journal of Physics **8**, 119 (2006).

[21] D. Giannios, "Prompt grb emission from gradual energy dissipation," Astronomy & Astrophysics **480**, 305–312 (2008).

[22] B. Zhang and H. Yan, "The internal-collision-induced magnetic reconnection and turbulence (ICMART) model of gamma-ray bursts," ApJ. **726**, 90 (2010).

[23] D. A. Uzdensky and J. C. McKinney, "Magnetic reconnection with radiative cooling. i. optically thin regime," Phys. Plasmas **18**, 042105 (2011).

[24] J. C. McKinney and D. A. Uzdensky, "A reconnection switch to trigger gamma-ray burst jet dissipation," Monthly Notices of the Royal Astronomical Society **419**, 573–607 (2012).

[25] Y. Lyubarsky and J. Kirk, "Reconnection in a striped pulsar wind," ApJ **547**, 437 (2001).

[26] D. A. Uzdensky and A. Spitkovsky, "Physical conditions in the reconnection layer in pulsar magnetospheres," ApJ **780**, 3 (2013).

[27] B. Cerutti, A. Philippov, K. Parfrey, and A. Spitkovsky, "Particle acceleration in axisymmetric pulsar current sheets," Monthly Notices of the Royal Astronomical Society **448**, 606–619 (2015).

[28] B. Cerutti, A. A. Philippov, and A. Spitkovsky, "Modelling high-energy pulsar light curves from first principles," Monthly Notices of the Royal Astronomical Society **457**, 2401–2414 (2016).

[29] A. A. Philippov and A. Spitkovsky, "Ab-initio pulsar magnetosphere: particle acceleration in oblique rotators and high-energy emission modeling," ApJ **855**, 94 (2018).

[30] V. L. Dorman and R. M. Kulsrud, "One-dimensional merging of magnetic fields with cooling," ApJ. **449**, 777 (1995).

[31] C. H. Jaroschek and M. Hoshino, "Radiation-dominated relativistic current sheets," Phys. Rev. Lett. **103**, 075002 (2009).

[32] B. Cerutti, G. R. Werner, D. A. Uzdensky, and M. C. Begelman, "Three-dimensional relativistic pair plasma reconnection with radiative feedback in the crab nebula," ApJ **782**, 104 (2014).

[33] J. Mehlhaff, G. Werner, D. Uzdensky, and M. Begelman, "Kinetic beaming in radiative relativistic magnetic reconnection: a mechanism for rapid gamma-ray flares in jets," Monthly Notices of the Royal Astronomical Society **498**, 799–820 (2020).

[34] J. Mehlhaff, G. Werner, D. Uzdensky, and M. Begelman, "Pair-regulated klein–nishina relativistic magnetic reconnection with applications to blazars and accreting black holes," Monthly Notices of the Royal Astronomical Society **508**, 4532–4572 (2021).

[35] K. M. Schoeffler, T. Grismayer, D. Uzdensky, R. Fonseca, and L. Silva, "Bright gamma-ray flares powered by magnetic reconnection in qed-strength magnetic fields," ApJ **870**, 49 (2019).

[36] K. Schoeffler, T. Grismayer, D. Uzdensky, and L. Silva, "High-energy synchrotron flares powered by strongly radiative relativistic magnetic reconnection: 2d and 3d pic simulations," Monthly Notices of the Royal Astronomical Society **523**, 3812–3839 (2023).

[37] L. Sironi and A. M. Beloborodov, "Kinetic simulations of radiative magnetic reconnection in the coronae of accreting black holes," ApJ **899**, 52 (2020).

[38] N. Sridhar, L. Sironi, and A. M. Beloborodov, "Comptonization by reconnection plasmoids in black hole coronae i: Magnetically dominated pair plasma," Monthly Notices of the Royal Astronomical Society **507**, 5625–5640 (2021).

[39] N. Sridhar, L. Sironi, and A. M. Beloborodov, "Comptonization by reconnection plasmoids in black hole coronae ii: Electron-ion plasma," Monthly Notices of the Royal Astronomical Society **518**, 1301–1315 (2023).

[40] H. Hakobyan, A. Philippov, and A. Spitkovsky, "Effects of synchrotron cooling and pair production on collisionless relativistic reconnection," ApJ **877**, 53 (2019).

[41] H. Hakobyan, B. Ripperda, and A. Philippov, "Radiative reconnection-powered tev flares from the black hole magnetosphere in m87," ApJ Letters **943**, L29 (2023).

[42] A. Oreshina and B. Somov, "Slow and fast magnetic reconnection. i. role of radiative cooling," Astron. Astrophys. **331**, 1078 (1998).

[43] A. A. Laguna, A. Lani, N. N. Mansour, H. Deconinck, and S. Poedts, "Effect of radiation on chromospheric magnetic reconnection: reactive and collisional multi-fluid simulations," ApJ. **842**, 117 (2017).

[44] L. Ni, V. S. Lukin, N. A. Murphy, and J. Lin, "Magnetic reconnection in strongly magnetized regions of the low solar chromosphere," ApJ. **852**, 95 (2018).

[45] L. Ni, V. S. Lukin, N. A. Murphy, and J. Lin, "Magnetic reconnection in the low solar chromosphere with a more realistic radiative cooling model," Phys. Plasmas **25**, 042903 (2018).

[46] N. Loureiro and D. Uzdensky, "Magnetic reconnection: from the sweet–parker model to stochastic plasmoid chains," Plasma Phys. Control. Fusion **58**, 014021 (2015).

[47] D. Uzdensky, N. Loureiro, and A. Schekochihin, "Fast magnetic reconnection in the plasmoid-dominated regime," Phys. Rev. Lett. **105**, 235002 (2010).

[48] M. Yamada *et al.*, "Study of driven magnetic reconnection in a laboratory plasma," Phys. Plasmas **4**, 1936–1944 (1997).

[49] H. Ji, M. Yamada, S. Hsu, R. Kulsrud, T. Carter, and S. Zaharia, "Magnetic reconnection with sweet-parker characteristics in two-dimensional laboratory plasmas," Phys. Plasmas **6**, 1743–1750 (1999).

[50] J. Olson, J. Egedal, S. Greess, R. Myers, M. Clark, D. Endrizzi, K. Flanagan, J. Milhone, E. Peterson, J. Wallace, *et al.*, "Experimental demonstration of the collisionless plasmoid instability below the ion kinetic scale during magnetic reconnection," Phys. Rev. Lett. **116**, 255001 (2016).

[51] J. Olson, J. Egedal, M. Clark, D. A. Endrizzi, S. Greess, A. Millet-Ayala, R. Myers, E. E. Peterson, J. Wallace, and C. B. Forest, "Regulation of the normalized rate of driven magnetic reconnection through shocked flux pileup," J. Plasma Phys. **87** (2021), 10.1017/S0022377821000659.

[52] S. C. Hsu, G. Fiksel, T. Carter, H. Ji, R. Kulsrud, and M. Yamada, "Local measurement of nonclassical ion heating during magnetic reconnection," Phys. Rev. Lett. **84**, 3859 (2000).

[53] Y. Ren, M. Yamada, S. Gerhardt, H. Ji, R. Kulsrud, and A. Kuritsyn, "Experimental verification of the hall effect during magnetic reconnection in a laboratory plasma," Phys. Rev. Lett. **95**, 055003 (2005).

[54] M. Rosenberg, C. Li, W. Fox, A. Zylstra, C. Stoeckl, F. Séguin, J. Frenje, and R. Petrasso, "Slowing of magnetic reconnection concurrent with weakening plasma inflows and increasing collisionality in strongly driven laser-plasma experiments," Phys. Rev. Lett. **114**, 205004 (2015).

[55] W. Fox, A. Bhattacharjee, and K. Germaschewski, "Magnetic reconnection in high-energy-density laser-produced plasmas," Phys. Plasmas **19**, 056309 (2012).

[56] P. Nilson *et al.*, "Magnetic reconnection and plasma dynamics in two-beam laser-solid interactions," Phys. Rev. Lett. **97**, 255001 (2006).

[57] C. Li *et al.*, "Observation of megagauss-field topology changes due to magnetic reconnection in laser-produced plasmas," Phys. Rev. Lett. **99**, 055001 (2007).

[58] W. Fox, G. Fiksel, D. B. Schaeffer, D. Haberberger, J. Matteucci, K. Lezhnin, A. Bhattacharjee, M. J. Rosenberg, S. X. Hu, A. Howard, D. Uzdensky, and K. Germaschewski, "A novel kinetic mechanism for the onset of fast magnetic reconnection and plasmoid instabilities in collisionless plasmas," arXiv (2021), 2112.03316.

[59] G. Fiksel, W. Fox, A. Bhattacharjee, D. Barnak, P.-Y. Chang, K. Germaschewski, S. Hu, and P. Nilson, "Magnetic reconnection between colliding magnetized laser-produced plasma plumes," Phys. rev. Lett. **113**, 105003 (2014).

[60] A. Chien, L. Gao, S. Zhang, H. Ji, E. G. Blackman, W. Daughton, A. Stanier, A. Le, F. Guo, R. Follett, *et al.*, "Non-thermal electron acceleration from magnetically driven reconnection in a laboratory plasma," Nature Physics **19**, 254–262 (2023).

[61] S. Lebedev, A. Frank, and D. Ryutov, "Exploring astrophysics-relevant magnetohydrodynamics with pulsed-power laboratory facilities," Reviews of Modern Physics **91**, 025002 (2019).

[62] L. Suttle, J. Hare, S. Lebedev, G. Swadling, G. Burdiak, A. Ciardi, J. Chittenden, N. Loureiro, N. Niasse, F. Suzuki-Vidal, *et al.*, "Structure of a magnetic flux annihilation layer formed by the collision of supersonic, magnetized plasma flows," Phys. Rev. Lett. **116**, 225001 (2016).

[63] J. Hare, L. Suttle, S. Lebedev, N. Loureiro, A. Ciardi, J. Chittenden, T. Clayson, S. Eardley, C. Garcia, J. Halliday, *et al.*, "An experimental platform for pulsed-power driven magnetic reconnection," Phys. Plasmas **25**, 055703 (2018).

[64] J. Hare, L. Suttle, S. Lebedev, N. Loureiro, A. Ciardi, G. Burdiak, J. Chittenden, T. Clayson, C. Garcia, N. Niasse, *et al.*, "Anomalous heating and plasmoid formation in a driven magnetic reconnection experiment," Phys. Rev. Lett. **118**, 085001 (2017).

[65] J. Hare, S. Lebedev, L. Suttle, N. Loureiro, A. Ciardi, G. Burdiak, J. Chittenden, T. Clayson, S. Eardley, C. Garcia, *et al.*, "Formation and structure of a current sheet in pulsed-power driven magnetic reconnection experiments," Phys. Plasmas **24**, 102703 (2017).

[66] L. G. Suttle, G. C. Burdiak, C. L. Cheung, T. Clayson, J. W. Halliday, J. D. Hare, S. Rusli, D. Russell, E. Tubman, A. Ciardi, *et al.*, "Interactions of magnetized plasma flows in pulsed-power driven experiments," Plasma Phys. Control. Fusion **62**, 014020 (2019).

[67] L. Suttle, J. Hare, S. Lebedev, A. Ciardi, N. Loureiro, G. Burdiak, J. Chittenden, T. Clayson, J. Halliday, N. Niasse, *et al.*, "Ion heating and magnetic flux pile-up in a magnetic reconnection experiment with super-alfvénic plasma inflows," Phys. Plasmas **25**, 042108 (2018).

[68] D. Sinars, M. Sweeney, C. Alexander, D. Ampleford, T. Ao, J. Apruzese, C. Aragon, D. Armstrong, K. Austin, T. Awe, *et al.*, "Review of pulsed power-driven high energy density physics research on z at sandia," Phys. Plasmas **27**, 070501 (2020).

[69] R. Datta, A. J. Crilly, J. P. Chittenden, S. Chowdhry, K. Chandler, N. Chaturvedi, C. E. Myers, W. R. Fox, S. B. Hansen, C. A. Jennings, H. Ji, C. C. Kuranz, S. V. Lebedev, D. A. Uzdensky, and J. D. Hare, "Simulations of radiatively cooled magnetic reconnection driven by pulsed power," arXiv (2024), 10.48550/arXiv.2401.01795, 2401.01795.

[70] J. Chittenden, S. Lebedev, B. Oliver, E. Yu, and M. Cuneo, "Equilibrium flow structures and scaling of implosion trajectories in wire array z pinches," Phys. Plasmas **11**, 1118–1127 (2004).

[71] A. Ciardi *et al.*, "The evolution of magnetic tower jets in the laboratory," Phys. Plasmas **14**, 056501 (2007).

[72] A. Crilly, N. Niasse, A. Fraser, D. Chapman, K. McLean, S. Rose, and J. Chittenden, "Spk: A fast atomic and microphysics code for the high-energy-density regime," High Energy Density Physics , 101053 (2023).

[73] R. Datta, K. Chandler, C. E. Myers, J. P. Chittenden, A. J. Crilly, C. Aragon, D. J. Ampleford, J. T. Banasek, A. Edens, W. R. Fox, S. B. Hansen, E. C. Harding, C. A. Jennings, H. Ji, C. C. Kuranz, S. V. Lebedev, Q. Looker, S. G. Patel, A. Porwitzky, G. A. Shipley, D. A. Uzdensky, D. A. Yager-Elorriaga, and J. D. Hare, "Plasmoid formation and strong radiative cooling in a driven magnetic reconnection experiment," arXiv (2024), 2401.04643.

[74] S. Lebedev, F. Beg, S. Bland, J. Chittenden, A. Dangor, and M. Haines, "Snowplow-like behavior in the implosion phase of wire array z pinches," Phys. Plasmas **9**, 2293–2301 (2002).

[75] R. Datta, J. Angel, J. Greenly, S. Bland, J. Chittenden, E. Lavine, W. Potter, D. Robinson, E. Wong, D. Hammer, *et al.*, "Plasma flows during the ablation stage of an over-massed pulsed-power-driven exploding planar wire array," Phys. Plasmas **30** (2023), 10.1063/5.0160893.

[76] A. L. Velikovich, I. V. Sokolov, and A. A. Esaulov, "Perfectly conducting incompressible fluid model of a wire array implosion," Phys. Plasmas **9**, 1366–1380 (2002).

[77] S. Lebedev, L. Suttle, G. Swadling, M. Bennett, S. Bland, G. Burdiak, D. Burgess, J. Chittenden, A. Ciardi, A. Clemens, *et al.*, "The formation of reverse shocks in magnetized high energy density supersonic plasma flows," Phys. Plasmas **21**, 056305 (2014).

[78] T. Webb, D. Bliss, G. Chandler, D. Dolan, G. Dunham, A. Edens, E. Harding, M. Johnston, M. Jones, S. Langendorf, *et al.*, "Radiation, optical, power flow, and electrical diagnostics at the z facility: Layout and techniques utilized to operate in the harsh environment," Review of Scientific Instruments **94** (2023), 10.1063/5.0123448.

[79] K. Swanson, G. Jaar, D. Mayes, R. Mancini, V. Ivanov, A. Astanovitskiy, O. Dmitriev, A. Klemmer, C. De La Cruz, D. Dolan, *et al.*, "Development and integration of photonic doppler velocimetry as a diagnostic for radiation driven experiments on the z-machine," Review of Scientific Instruments **93** (2022), 10.1063/5.0084638.

[80] T. Byvank, J. Banasek, W. Potter, J. Greenly, C. Seyler, and B. Kusse, "Applied axial magnetic field effects on laboratory plasma jets: Density hollowing, field compression, and azimuthal rotation," Phys. Plasmas **24** (2017), 10.1063/1.3079752.

[81] G. Burdiak, S. Lebedev, S. Bland, T. Clayson, J. Hare, L. Suttle, F. Suzuki-Vidal, D. Garcia, J. Chittenden, S. Bott-Suzuki, *et al.*, "The structure of bow shocks formed by the interaction of pulsed-power driven magnetised plasma flows with conducting obstacles," Phys. Plasmas **24**, 072713 (2017).

[82] R. Datta, D. R. Russell, I. Tang, T. Clayson, L. G. Suttle, J. P. Chittenden, S. V. Lebedev, and J. D. Hare, "The structure of 3-d collisional magnetized bow shocks in pulsed-power-driven plasma flows," J. Plasma Phys. **88**, 905880604 (2022).

[83] R. Datta, D. Russell, I. Tang, T. Clayson, L. Suttle, J. Chittenden, S. Lebedev, and J. Hare, "Time-resolved velocity and ion sound speed measurements from simultaneous bow shock imaging and inductive probe measurements," Review of Scientific Instruments **93**, 103530 (2022).

[84] M. Schaeuble *et al.*, "Experimental methods for laboratory measurements of helium spectral line broadening in white dwarf photospheres," Phys. Plasmas **28**, 062902 (2021).

[85] E. Harding, T. Ao, J. Bailey, G. Loisel, D. Sinars, M. Geissel, G. Rochau, and I. Smith, "Analysis and implementation of a space resolving spherical crystal spectrometer for x-ray thomson scattering experiments," Review of Scientific Instruments **86** (2015), 10.1063/1.4918619.

[86] G. Herzberg and J. W. T. Spinks, *Atomic spectra and atomic structure* (Courier Corporation, 1944).

[87] I. I. Sobelman, *Atomic spectra and radiative transitions*, Vol. 12 (Springer Science & Business Media, 2012).

[88] R. Drake, *High-Energy-Density Physics* (Springer, 2013).

[89] J. MacFarlane, I. Golovkin, P. Woodruff, S. Kulkarni, and I. Hall, "Simulation of plasma ionization and spectral properties with prismspect," 2013 Abstracts IEEE International Conference on Plasma Science (ICOPS) , 1–1 (2013).

[90] R. Datta, F. Ahmed, and J. D. Hare, "Machine learning assisted analysis of visible spectroscopy in pulsed-power-driven plasmas," arXiv preprint arXiv:2308.16828 (2023), 10.48550/arXiv.2308.16828.

[91] D. R. Russell, G. C. Burdiak, J. J. Carroll-Nellenback, J. Halliday, J. Hare, S. Merlini, L. G. Suttle, V. Valenzuela-Villaseca, S. Eardley, J. A. Fullalove, *et al.*, "Perpendicular subcritical shock structure in a collisional plasma experiment," Phys. Rev. Lett. **129**, 225001 (2022).

[92] S. Lebedev, D. Ampleford, S. Bland, S. Bott, J. Chittenden, C. Jennings, M. Haines, J. Palmer, and J. Rapley, "Implosion dynamics of wire array z-pinches: experiments at imperial college," Nuclear fusion **44**, S215 (2004).

[93] J. T. Knudtson, W. B. Green, and D. G. Sutton, "The uv-visible spectroscopy of laser-produced aluminum plasmas," Journal of Applied physics **61**, 4771–4780 (1987).

[94] J. Bailey, G. Rochau, R. Mancini, C. Iglesias, J. MacFarlane, I. Golovkin, J. Pain, F. Gilleron, C. Blancard, P. Cosse, *et al.*, "Diagnosis of x-ray heated mg/fe opacity research plasmas," Review of Scientific Instruments **79** (2008), https://doi.org/10.1063/1.3020710.

[95] A. Crilly, *Simulation of nuclear observables in inertial confinement fusion experiments*, Ph.D. thesis, Imperial College London (2020).

[96] We also solve the 1D radiation transport equation (Equation 1) to determine the filtered intensity of radiation from the emitting plasma, and the conclusions presented here are consistent with that seen from the emissivity in Figure 12c.

[97] N. Loureiro, A. Schekochihin, and S. Cowley, "Instability of current sheets and formation of plasmoid chains," Phys. Plasmas **14**, 100703 (2007).

[98] S. Hansen, J. Bauche, C. Bauche-Arnoult, and M. Gu, "Hybrid atomic models for spectroscopic plasma diagnostics," High Energy Density Physics **3**, 109–114 (2007).

[99] J. P. Goedbloed, R. Keppens, and S. Poedts, *Advanced Magnetohydrodynamics: With Applications to Laboratory and Astrophysical Plasmas* (Cambridge University Press, 2010).

[100] A. Richardson, *NRL plasma formulary* (US Naval Research Laboratory, 2019).

[101] W. Fox, A. Bhattacharjee, and K. Germaschewski, "Fast magnetic reconnection in laser-produced plasma bubbles," Phys. Rev. Lett. **106**, 215003 (2011).

A. Appendix A

In this Appendix, we provide a detailed discussion of how the parameters required to calculate terms in the energy equation (Equation 3) can be estimated at $t = 220\,\mathrm{ns}$, which is the time of peak X-ray emission. Based on the measured values of ion density n_i, electron temperature T_e (see §IV B), magnetic field B, and flow velocity V (see §II B 2) in the inflow region, we find that the inflows are super-Alfvénic ($M_A = V/V_A \approx 7$). We reiterate that these quantities are measured on the side of the array opposite the reconnection layer. Therefore, by taking advantage of the azimuthal symmetry of the outflows from the arrays (which form the inflows to the layer), we diagnose the inflow conditions, unaffected by the reconnection process. Other relevant quantities, such as the thermal pressure $p = (\bar{Z}+1)n_iT_e$, adiabatic index γ,[88] sound speed $C_S = \sqrt{\gamma p/\rho}$, thermal $\beta = p/(B^2/2\mu_0)$ and kinetic $\beta_{kin} = \rho V^2/(B^2/\mu_0)$ betas, the ion skin depth d_i,[100] ion-ion collisional mean free path λ_{ii},[100] and the ion-electron energy equilibriation time τ_E,[100] in this inflow region can be calculated from these measured parameters, and are shown in column 1 of Table II.

TABLE II: Plasma parameters at the time of peak X-ray emission (220 ns). Bold values are measured experimentally, while others are estimated/inferred. In column 1, we report values of n_i, T_e, and $\bar{Z}$ from visible spectroscopy analysis at 8 mm from the wires (see §IV B), magnetic field from averaging the values recorded by the inductive probes at 5 mm and 10 mm in MARZ3 (Figure 3c), and the flow velocity is estimated from the transit time of the magnetic field between the two probes (Figure 4d). Parenthetical values show bounds from X-ray spectroscopy (§IV E)

Parameter	**Pre-shock**	**Post-shock**	**Reconnection**
	Inflow	**Inflow**	**Layer**
$n_i\,[\times 10^{18}\,\mathrm{cm}^{-3}]$	**0.8**	6	6 ($\lesssim$ **5**)
T_e [eV]	**1.9**	30	60 ($\lesssim$ **75**)
$\bar{Z}$	**2**	8	10
B_y [T]	**3.9**	30	-
p [MPa]	0.6	300	700
V_x [km/s]	**140**	20	-
V_y [km/s]	-	-	**72**
V_A [km/s]	20	50	-
C_S [km/s]	5	30	50
β	0.1	0.8	-
β_{kin}	60	0.1	-
γ	1.2	1.1	1.1
d_i [mm]	0.7	0.1	0.1
λ_{ii} [nm]	20	1	1
S_L	-	-	120
τ_E [ns]	2	1	1

Super-Alfvénic inflows have previously been shown to generate shock-mediated magnetic flux pile-up upstream of the reconnection layer, dividing the inflow into pre-shock and post-shock pile-up regions.[51,62,67,101] In simulations of the MARZ experiment, magnetic flux pile-up results in fast perpendicular MHD shocks upstream of the reconnection layer.[69] Although we do not have diagnostics in MARZ1-3 to directly diagnose shock formation, we expect shocks to form upstream of the layer based on previous experimental work[62,67] and simulations[69] with strongly driven inflows. Ref. 73 estimates the parameters in the post-shock inflow region by solving the Rankine-Hugoniot jump conditions, the solution to which is a function of the upstream M_A, plasma beta β, and adiabatic index γ.[99] The plasma parameters in the pre-shock and post-shock inflow regions are listed in the first and second columns of Table II.

The plasma properties in the post-shock pile-up region set the inflow conditions just outside the reconnection layer. Ref. 73 uses two additional assumptions, both supported by simulation results, to approximate properties in the reconnection layer — (1) the reconnection layer exists in pressure balance with the post pile-up inflow region; and (2) at 220 ns, the layer mass density is roughly equal to that in the post-shock inflow region. The first assumption simply states that the kinetic $\rho_{in} V_{in}^2/2$, magnetic $B_{in}^2/2\mu_0$ and thermal p_{in} pressures just outside the reconnection layer must be balanced by the thermal pressure p_L inside the layer. The second assumption argues that the temperature of the layer T_L has not fallen enough at 220 ns to cause a significant increase in the layer density relative to the inflow density. The estimated plasma properties in the reconnection layer are listed in the third column of Table II.

We note that the estimated layer temperature at this time is $T_{bulk} \approx 60\,\mathrm{eV}$, which is consistent with the upper bound ($T_{e,bulk} \lesssim 75\,\mathrm{eV}$) determined from X-ray spectroscopy (§IV E), and the predicted ion density is $n_i \approx 6 \times 10^{18}\,\mathrm{cm}^{-3}$, slightly greater than the upper bound of $n_i \lesssim 5 \times 10^{18}\,\mathrm{cm}^{-3}$) from X-ray spectroscopy. The estimated Lundquist number is $S_L = LV_A/\bar{\eta} \approx 120$, and the predicted Sweet-Parker layer half-width is $\delta_{SP} \approx L(S_L)^{1/2} \approx 1.4\,\mathrm{mm}$,[3,11] which is comparable to the FWHM$= 1.6 \pm 0.5\,\mathrm{mm}$ of the X-ray emission region observed in the time-integrated image of the reconnection layer (Figure 8c). We approximate the layer half-length $L = 15\,\mathrm{mm}$, using half the radius of curvature of the magnetic field lines at the mid-plane. Lastly, an estimate of the reconnection rate is determined by comparing the post-shock inflow velocity $V_{in} \approx 20\,\mathrm{km\,s^{-1}}$ to the outflow velocity $V_{out} \approx 72\,\mathrm{km\,s^{-1}}$, estimated by extrapolating the linear trend in the hotspot velocity observed in Figure 9. The inferred reconnection rate at this time is $V_{in}/V_{out} \approx 0.3$. This is roughly comparable to the expected reconnection rate from Sweet-Parker theory $S_L^{-1/2} \approx 0.1$.[11]